

High Resolution, Differential, Near-infrared Transmission Spectroscopy of GJ 1214b

I. J. M. Crossfield¹, Travis Barman², Brad M. S. Hansen¹

ABSTRACT

The nearby star GJ 1214 hosts a planet intermediate in radius and mass between Earth and Neptune, resulting in some uncertainty as to its nature. We have observed this planet, GJ 1214b, during transit with the high-resolution, near-infrared NIRSPEC spectrograph on the Keck II telescope, in order to characterize the planet’s atmosphere. By cross-correlating the spectral changes through transit with a suite of theoretical atmosphere models, we search for variations associated with absorption in the planet atmosphere. Our observations are sufficient to rule out tested model atmospheres with wavelength-dependent transit depth variations $\gtrsim 5 \times 10^{-4}$ over the wavelength range 2.1 – 2.4 μm . Our sensitivity is limited by variable slit loss and telluric transmission effects.

We find no positive signatures but successfully rule out a number of plausible atmospheric models, including the default assumption of a gaseous, H-dominated atmosphere in chemical equilibrium. Such an atmosphere can be made consistent if the absorption due to methane is reduced. Clouds can also render such an atmosphere consistent with our observations, but only if they lie higher in the atmosphere than indicated by recent optical and infrared measurements.

When taken in concert with constraints from other groups, our results support a consensus model in which the atmosphere of GJ 1214b contains significant H and He, but where CH_4 is depleted. If this depletion is the result of photochemical processes, it may also produce a haze that suppresses spectral features in the optical.

Subject headings: infrared: stars — planetary systems — stars: individual (GJ 1214) — techniques: spectroscopic

1. Introduction

1.1. Characterizing Extrasolar Atmospheres

Astronomers are poised to soon discover the first rocky, Earth-like exoplanets orbiting in the habitable zone – the region where water could be expected to be liquid on the planet’s surface. Already,

¹Department of Physics & Astronomy, University of California Los Angeles, Los Angeles, CA 90095, USA, ianc@astro.ucla.edu

²Lowell Observatory, 1400 West Mars Hill Road, Flagstaff, AZ 86001, USA

ground-based exoplanet surveys are finding Super Earths (planets several times Earth’s mass and radius) such as GJ 1214b with temperatures only a few hundred degrees hotter than Earth (Charbonneau et al. 2009) – much more hospitable than the more easily detected giant, highly irradiated Hot Jupiters. In addition, the *Kepler* spacecraft is currently searching for the subtle, periodic dip in a star’s brightness that will indicate an Earth-sized planet in an Earth-like orbit has passed in front of its Sun-like stellar host, and indeed a preliminary list of 54 habitable planet candidates has already been released (Borucki et al. 2011).

Transit and radial velocity measurements can constrain the radius and mass of a planet, but significant degeneracies remain in the determination of interior and atmospheric composition. From theoretical models of planetary interiors we know that any Jupiter-sized object is composed primarily of H₂ and He. A Super Earth is more complicated and thus more interesting: it could be a small, rocky core with an extended H₂/He envelope (a mini-Neptune), a larger, icy core with a denser molecular atmosphere (a scaled-up Ganymede), or something in between (Rogers & Seager 2010). To determine the true makeup of such a planet we need precise methods to characterize the atmospheres of these new worlds.

All else being equal, planets which transit small, low-mass stars are the most favorable targets for atmospheric characterization because the planet/star size ratio R_P/R_* is especially high. When the host star occults the planet one can measure the planet’s intrinsic emission spectrum; when the planet transits its star, the transit depth will vary with wavelength in a way that reflects absorption in the atmosphere at the limb of the planet. This quantity, $(R_P(\lambda)/R_*)^2$, is often called the transmission spectrum of the planet. The wavelength-dependent atmospheric signature during transit is a variable function of wavelength, but in general is proportional to the relative area of the atmospheric annulus probed, i.e. $HR_P(\lambda)/R_*^2$, where H is the standard atmospheric scale height (Miller-Ricci et al. 2009). In the most favorable cases the transmission spectrum’s features vary by $\sim 10^{-3}$ relative to the flux from the planet’s host star – challenging to detect, but much more tractable than the expected planet/star flux contrast of $\lesssim 10^{-4}$ from a relatively temperate planet.

While numerous transit observations have been made from space, it is only in the last few years that ground-based infrared characterization has met with success. Ground-based infrared photometry is becoming almost commonplace (e.g., Rogers et al. 2009; Croll et al. 2011a), but ground-based spectroscopy remains challenging. Swain et al. (2010) reported the detection of the K and L band emission spectrum of HD 189733b, but these results are contested (Madhusudhan & Seager 2009; Mandell et al. 2011). On a more optimistic note, the recently reported detection of CO on HD 209458b (Snellen et al. 2010) demonstrates the power of template cross-correlation techniques for ground-based spectroscopy. We will adopt a similar philosophy in this paper.

Recent observations of the low mass planet GJ 1214b represent some of the most precise ground-based exoplanet spectroscopy to date (Bean et al. 2010), and show a flat transmission spectrum from 0.75 – 1 μm . Our study aims to complement these results in the near-infrared. In this paper we describe our observations of GJ 1214b in an attempt to detect the differential transmission spectrum of the planet’s atmosphere. We describe the GJ 1214 system and the suite of atmospheric models we test in Section 2. We discuss our observations and data reduction in Section 3, and describe our methods for measuring relative spectrophotometry and performing model template cross-correlations in Section 4.

We finish with a discussion of our results and future work in Section 5 and conclude in Section 6.

2. Observations and Atmospheric Models

2.1. The GJ 1214 System

GJ 1214b is the first planet discovered by the M_{Earth} project (Irwin et al. 2009), a transit survey targeting the nearest red dwarfs. The planet orbits a 3000 K, M4.0-4.5 dwarf with high metallicity (+0.3 to +0.4; Schlaufman & Laughlin 2010; Rojas-Ayala et al. 2010). Because the star is so cool, the system is most amenable to characterization at infrared wavelengths. With a semimajor axis of 0.014 AU, the planet’s (albedo-dependent) equilibrium temperature is ~ 400 -550 K.

GJ 1214b’s size and mass (2.65 and 6.45 times that of the Earth, respectively; Carter et al. 2010) give it a density intermediate to that of our solar system’s inner (rocky) and outer (gas-dominated) planets. GJ 1214b occupies an intriguing location in the planetary mass-radius diagram, inasmuch as these two bulk characteristics allow for substantial degeneracies in models of the planet’s interior composition. Nonetheless, models generally suggest that the planet has a substantial gas component, making it potentially amenable to atmospheric characterization (Rogers & Seager 2010; Nettelmann et al. 2010).

Though the present constraints on GJ 1214b’s bulk composition preclude any unique predictions of the planet’s atmospheric structure and composition, Miller-Ricci & Fortney (2010) predicted that the planet would show substantial ($\sim 10^{-3}$) variations in transit depth with wavelength if it hosts a cloudless, H₂/He-dominated atmosphere. They also predicted that the atmospheric signature would be an order of magnitude lower – essentially undetectable in the near-infrared – for a denser atmosphere dominated by heavier molecular species. Any clouds in GJ 1214b’s atmosphere would further mask the presence of any spectral signals.

The planet to star size ratio R_P/R_* of the GJ 1214 system has been measured photometrically in the optical (Charbonneau et al. 2009; Carter et al. 2010) and mid-infrared (Désert et al. 2011) and with optical spectroscopy (Bean et al. 2010). These measurements all agree to within $\lesssim 2\%$, and have been interpreted as evidence for a clear atmosphere dominated by heavy molecular species (Désert et al. 2011). An atmosphere obscured by clouds or haze would also be consistent with these observations, but a haze would need to be composed of rather large (several microns) particles to flatten the spectrum all the way into the mid-infrared (Désert et al. 2011). On the other hand, recent measurements in the near infrared (Croll et al. 2011b) argue for a larger radius at Ks-band, indicative of a H-dominated atmosphere with large scale height. One way to make the observations consistent with one another is to postulate a methane-depleted atmosphere with a haze of small particles at $R_P/R_* \sim 0.1165$ to smooth out features in the optical (Désert et al. 2011; Croll et al. 2011b).

2.2. Atmospheric Models of GJ 1214b

We test our observations (described in Section 3) by comparing them to high-resolution model transmission spectra. Thus our detection method is only as good as the molecular line lists we use for our models: significant revision of the near-infrared opacities would require a recalculation of the constraints we ultimately present.

To explore a variety of atmospheric conditions in GJ 1214b we generated several irradiated planetary models using the PHOENIX code, assuming traditional H₂/He-rich atmospheres (Barman et al. 2005). The baseline models were taken to be cloud free with either solar (Asplund 2005), 10× solar, or 30× solar abundances (i.e., the abundance of all elements other than H and He enhanced by the specified factor), and we used the bulk planet and star parameters from Charbonneau et al. (2009).

We generated the following atmospheric models:

- Solar composition and equilibrium chemistry.
- 10× solar abundance and equilibrium chemistry. This model has a slightly smaller radius, and is hotter below 0.1 mbar, than the solar model.
- 30× solar abundance and equilibrium chemistry. This model has a slightly higher temperature and smaller radius than the solar and 10× solar models.
- No methane. Solar composition, but with the concentration of CH₄ set to zero. We used this model to interpolate to various levels of atmospheric CH₄. This allows us to test the hypothesis that CH₄ abundances may be substantially reduced in cooler atmospheres at the pressures probed by transmission spectroscopy (Zahnle et al. 2009; Désert et al. 2011).
- Low carbon abundance. This model assumes chemical equilibrium but with the carbon abundance set to 10^{−8} relative to solar. It is similar to the methane-depleted model just described, but features from residual CH₄ are still visible from 2.2-2.35 μm.

We plot the temperature-pressure (T/P) profiles and the abundance of several molecular species as a function of altitude for several of these models in Figure 1.

For each model we compute the monochromatic planetary radii, $R_P(\lambda)$, with PHOENIX under the assumption of spherical symmetry (Barman 2007) and with a wavelength sampling of 0.05 Å from 1 – 3 μm. Each radius spectrum is then convolved with a Gaussian kernel to the instrumental resolution and then interpolated onto the observed wavelengths. We also compute the quantity σ_{R_P} , defined as the standard deviation of the planet radius at our model resolution over the wavelength range used in our analysis. A completely flat spectrum would have $\sigma_{R_P} = 0$ and be undetectable by our methods, but models with sufficiently prominent spectral features – which we can detect – have larger values. To facilitate comparison of σ_{R_P} with our sensitivity limits we list these values in Table 4 with the final results of our analysis.

Note that all of our models are H₂/He-dominated. There are many possible alternative compositions (Miller-Ricci & Fortney 2010; Rogers & Seager 2010), but the atmospheric scale heights of those dominated by heavier molecules result in suppressed transmission spectra with features undetectable at our precision. We list some of the models we test, and the $R_P(\lambda)$ they predict when observed with

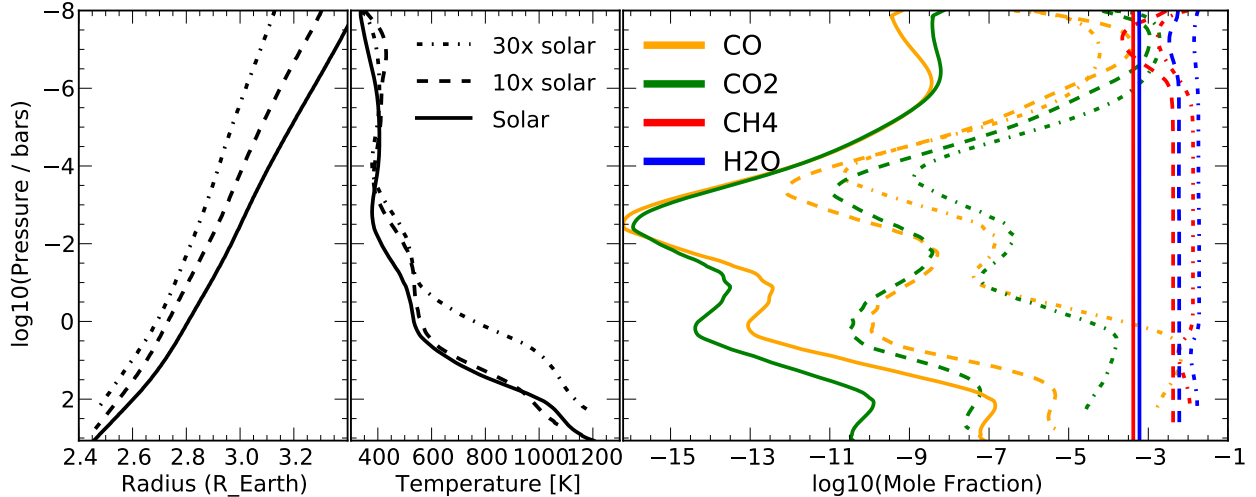


Fig. 1.— Atmospheric parameters for our solar (dot-dashed), $10\times$ solar (dashed), and $30\times$ solar (solid) abundance models. From left to right, the panels show as a function of altitude: the effective planetary radii, the temperature-pressure profiles, and the abundances of several species. We discuss our models in Section 2.2, and show transmission spectra in Figure 2 and 3.

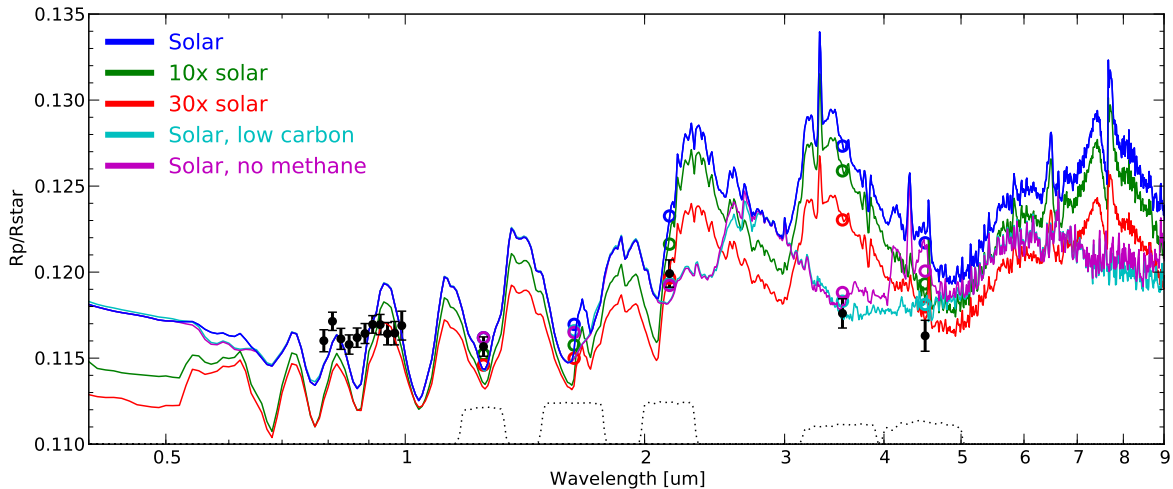


Fig. 2.— A selection of our model transmission spectra of GJ 1214b (solid lines; smoothed for display purposes). The dashed lines at bottom represents the effective throughput of the WIRCcam J, H, and Ks and IRAC 1 & 2 filters. The open circles show the averages of our models over the several filters, and the solid points are the observations (Bean et al. 2010; Désert et al. 2011; Croll et al. 2011b). The spectroscopic analysis presented in this paper rules out all but the low carbon and no methane models (cf. Table 4). We describe these models in Section 2.2 and Table 1.

CFHT/WIRCcam at J, H, and Ks, and with Spitzer/IRAC CH1 ($3.6\ \mu\text{m}$) and CH2 ($4.5\ \mu\text{m}$), in Table 1. We plot $R_P(\lambda)$ from a selection of our models in Figure 2 across the near-infrared, and in Figure 3 zoomed in on the spectral regions probed by our NIRSPEC observations.

In the infrared, as in the optical, clouds can alter the transit spectrum by blocking flux below a certain radius, establishing different minimum radii compared to cloud-free models. The impact of cloud opacity was tested for the cloud-free models described above by truncating the model radius spectrum

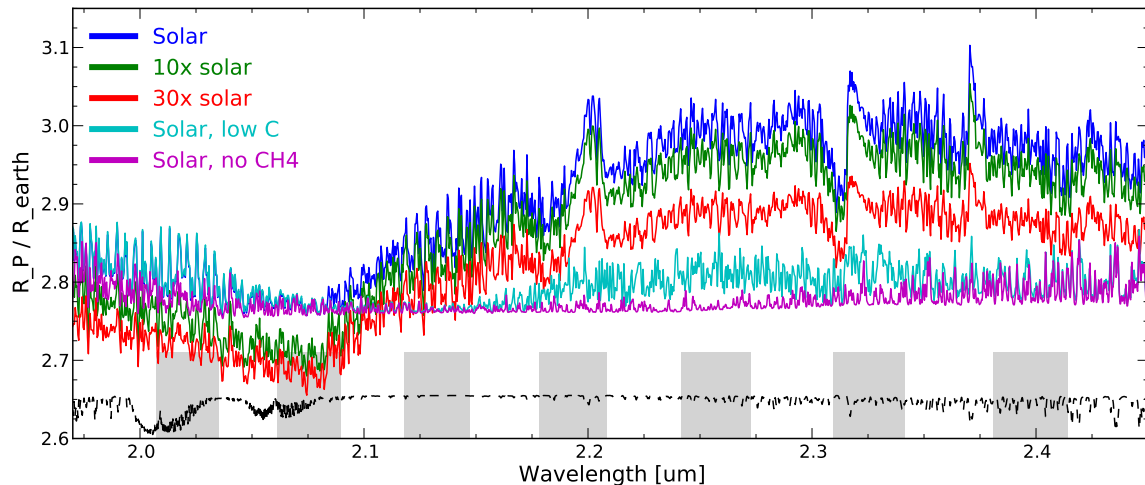


Fig. 3.— A selection of the same model transmission spectra shown in Figure 2, showing only the wavelength range covered by our observations and smoothed for display purposes. The shaded regions represents those wavelength we observed; the regions are discontinuous due to NIRSPEC’s echelle format. The dashed line represents the telluric transmission (Hinkle et al. 2003).

at several different values, in effect inserting an opaque cloud deck at a desired level in the atmosphere. This means that in our cloudy cases we set all values of $R_P(\lambda)$ less than a given radius equal to that radius.

3. NIRSPEC Observations and Analysis

3.1. Summary of Observations

The temperature of GJ 1214b is such that we expect many prominent spectral features in the near infrared, and we therefore observed GJ 1214b using the NIRSPEC cryogenic near-infrared echelle spectrograph (McLean et al. 1998), located at the Nasymth focus of the Keck II telescope. Our observations covered one transit each in both the H and K near-infrared bands; we list the details of these observations and our instrumental setup in Table 2.

On both nights we observed the GJ 1214 system continuously for as long as conditions permitted. We designed our observations to minimize possible sources of systematic error, and thus did not nod the telescope. Our prior experience with NIRSPEC and with SpeX (a moderate-resolution spectrograph at the NASA Infrared Telescope Facility) has taught us that nodding induces an undesirable “sawtooth” pattern in the extracted spectrophotometry (presumably due to residual flat-field variations), while it does not provide a substantial improvement in removing background emission. Instead, we kept the target star in a fixed position about 6” from the end of the spectrograph slit; this allowed us to squeeze an extra echelle order onto the detector. For the same reason, we deactivated the instrument’s field rotator; differential atmospheric refraction did not appear to affect the relative tilt of our spectra over the course of the night. We used the widest possible slit (0.7”) to maximize throughput and minimize the effects of sub-arcsecond guiding errors. Typical frames had maximum count rates of $\sim 5,000 e^-$ per

Table 1. GJ 1214b Predicted Photometric Transit Radii (cf. Figure 2)

Model	R_{min}^a / R_{\oplus}	J ^b	H ^b	Ks ^b	IRAC1 (3.6 μm)	IRAC2 (4.5 μm)
Solar	-	2.665	2.683	2.828	2.921	2.792
Solar	2.85	2.850	2.850	2.877	2.921	2.851
Solar	2.90	2.900	2.900	2.909	2.931	2.900
10x solar	-	2.643	2.656	2.790	2.888	2.737
10x solar	2.85	2.850	2.850	2.865	2.892	2.850
10x solar	2.90	2.900	2.900	2.901	2.911	2.900
30x solar	-	2.629	2.638	2.745	2.823	2.707
Solar, low carbon	-	2.665	2.675	2.737	2.714	2.710
Solar, no methane	-	2.665	2.673	2.735	2.726	2.754

^aPlanetocentric radius of artificially imposed near-infrared opaque cloud deck; cf. Section 2.2

^bNear-infrared radii computed using the CFHT/WIRCcam filter profiles at <http://www.cfht.hawaii.edu/Instruments/Filters/wircam.html>

Table 2. Observations

	2010 Aug 16	2010 Sep 04
Cross-disperser position	35.60	36.89
Echelle position	63.82	62.94
Slit	0.72" x 24"	0.72" x 12"
Filter	NIRSPEC-7	NIRSPEC-5
Wavelength coverage (μm)	2.007 - 2.414	1.514 - 1.783
Spectral grasp	52%	70%
Integration Time (sec)	60	60
Number of co-adds	1	1
Number of exposures	182	85
Airmass range	1.04 - 1.65	1.15 - 1.65
GJ 1214b phase coverage	-0.060 - +0.038	-0.021 - +0.025

pixel, safely within the ALADDIN-3 detector’s linear response range. We chose not to switch repeatedly between target and calibrator stars because (a) of the limited amount of observation time (GJ 1214b’s transit only lasts about an hour), and (b) in our experience each re-acquisition of the target can induce substantial flux discontinuities in spectrophotometric time series.

3.2. Initial Data Reduction

We reduce the raw echellegrams using a combination of standard IRAF routines (as implemented in PyRAF¹) and our own set of Python analysis tools²; we also draw on the experience of similar past observations (e.g., Deming et al. 2005). We dark-subtract and flat-field the frames, and interpolate over cosmic rays and bad pixels. The two left-hand (shorter-wavelength) quadrants of the NIRSPEC detector sometimes exhibit nonuniform readout characteristics in a pattern that repeats every eight detector rows. This manifests itself both as increased read noise and an apparent bias offset in affected rows. We remove the offset from each set of rows in each quadrant using linear least squares after excluding pixel values more than seven standard deviations from the median. Nonetheless the short-wavelength half of each extracted echelle order is detectably noisier.

We extract the spectra using the standard IRAF `apall` task with variance weighting and a third-order sky background fit. Our extraction ignores the slight tilt of the spectrograph slit in the raw spectral orders, but this does not seriously compromise our resolution ($R \sim 17,000$) when using the 0.7” slit. The extracted spectra have fluxes of $\sim 16,000 \text{ e}^- \text{ pix}^{-1}$. After removing observations rendered unusable for telescope or instrumental reasons (e.g., loss of guiding or server crashes), we are left with 182 K-band and 85 H-band spectra.

Our initial analysis reveals that the the H-band data are unable to constrain the presence of even the most easily detectable atmospheric models. The cause seems to be the relatively short duration of the H band data (cf. Table 2), and especially the paucity of out-of-transit observations. We repeated the analysis we describe below using only 80 of the 182 K-band frames (similar in length to the H band data set); under these conditions we achieve precision comparable to that from the H band dataset. Therefore it seems likely that the limiting factor in the H band data set is an insufficient number of observations and/or insufficient pre- and post-transit coverage. We thus discard the H band data and focus solely on the K band data.

We calculate a wavelength solution for our spectra using the IRAF task `ecidentify` to identify isolated telluric absorption lines in each extracted spectrum. As our reference we use the high-resolution telluric absorption spectrum measured by Hinkle et al. (2003). We fit a third-order dispersion solution to all echelle orders simultaneously; our final wavelength solution has RMS residuals of 0.1 Å.

To convert observed wavelengths to wavelengths in the GJ 1214 system’s rest frame we use a radial velocity of 48 km s^{-1} , which we estimate by cross-correlating a high-resolution model stellar spectrum

¹PyRAF is a command language for running IRAF tasks that is based on the Python scripting language, and is available at http://www.stsci.edu/resources/software_hardware/pyraf/

²Available at <http://www.astro.ucla.edu/~ianc/>

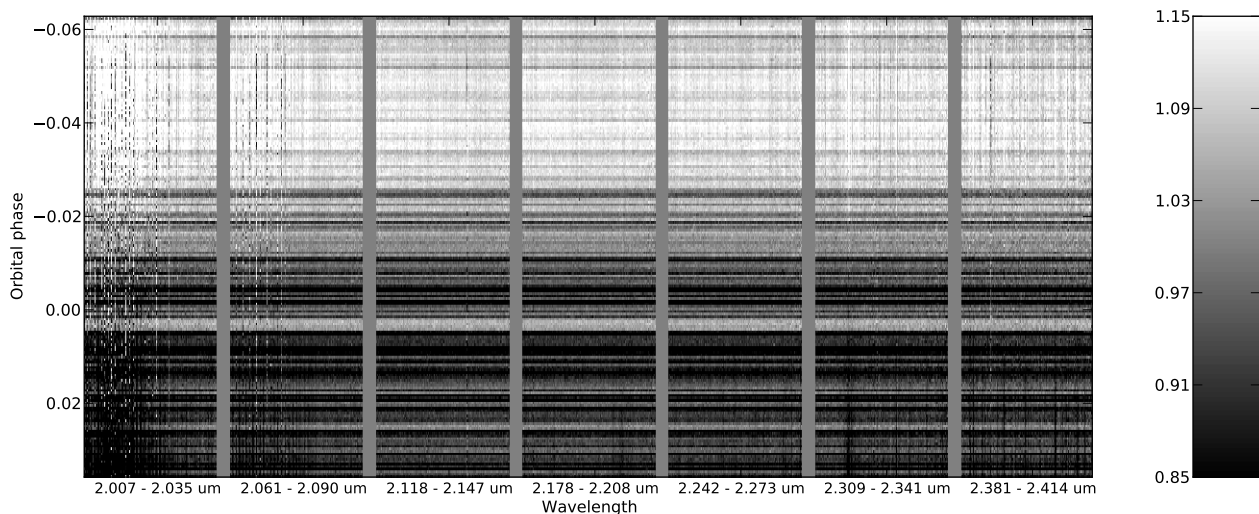


Fig. 4.— Spectrophotometric data $f_{i\lambda}$, normalized by the median value in each wavelength channel. The variations (due to a combination of airmass effects and instrumental slit loss) are of order 10% (which prevents us from directly seeing GJ 1214b’s transit) and are largely common mode. For display purposes the data from each echelle order are separated by a narrow gray region.

with our spectra. Before cross-correlation we used the IDL package XTELLCORR (Vacca et al. 2003) to correct our GJ 1214 spectra for telluric absorption using observations we took of the A0V star HD 161289. Finally, we convert the UTC timestamps in our NIRSPEC files to heliocentric Julian dates (HJD) using the function `helio_jd` in the Python `astrolib` module.

3.3. Measuring systematic effects

Our spectra, shown in Figure 4, exhibit substantial residual temporal variations due to a combination of instrumental, telluric, and astrophysical sources (i.e., the planetary transit), with the latter the weakest of these effects. We wish to quantify and ultimately remove the instrumental and telluric effects to the extent that we can convincingly detect any wavelength-dependent variations in the transit depth.

The widest slit available on NIRSPEC is only 0.7” across, so even in excellent seeing significant light is lost and does not enter the slit. In 0.6” seeing (about the best we observed), guiding errors of 0.1” can cause the amount of light entering the spectrograph to vary by $\sim 10\%$. We see variations at this level in our spectrophotometric data, which we attribute to pointing jitter. These variations wholly overwhelm the $\sim 1\%$ flux decrement from GJ 1214b’s transit.

We quantify the amount of light coupled into the spectrograph slit by measuring the flux in spectral regions free of telluric absorption lines; we avoid these lines by referring to a high-resolution telluric absorption spectrum (Hinkle et al. 2003). We list the spectral regions we use in Table 3. The flux in these channels should only depend on (a) frame-to-frame changes in starlight entering the spectrograph slit, and (b) atmospheric continuum extinction. In each spectrum we add up the flux in these telluric-free regions, creating a time series representative of the slit losses suffered by the instrument. We denote this

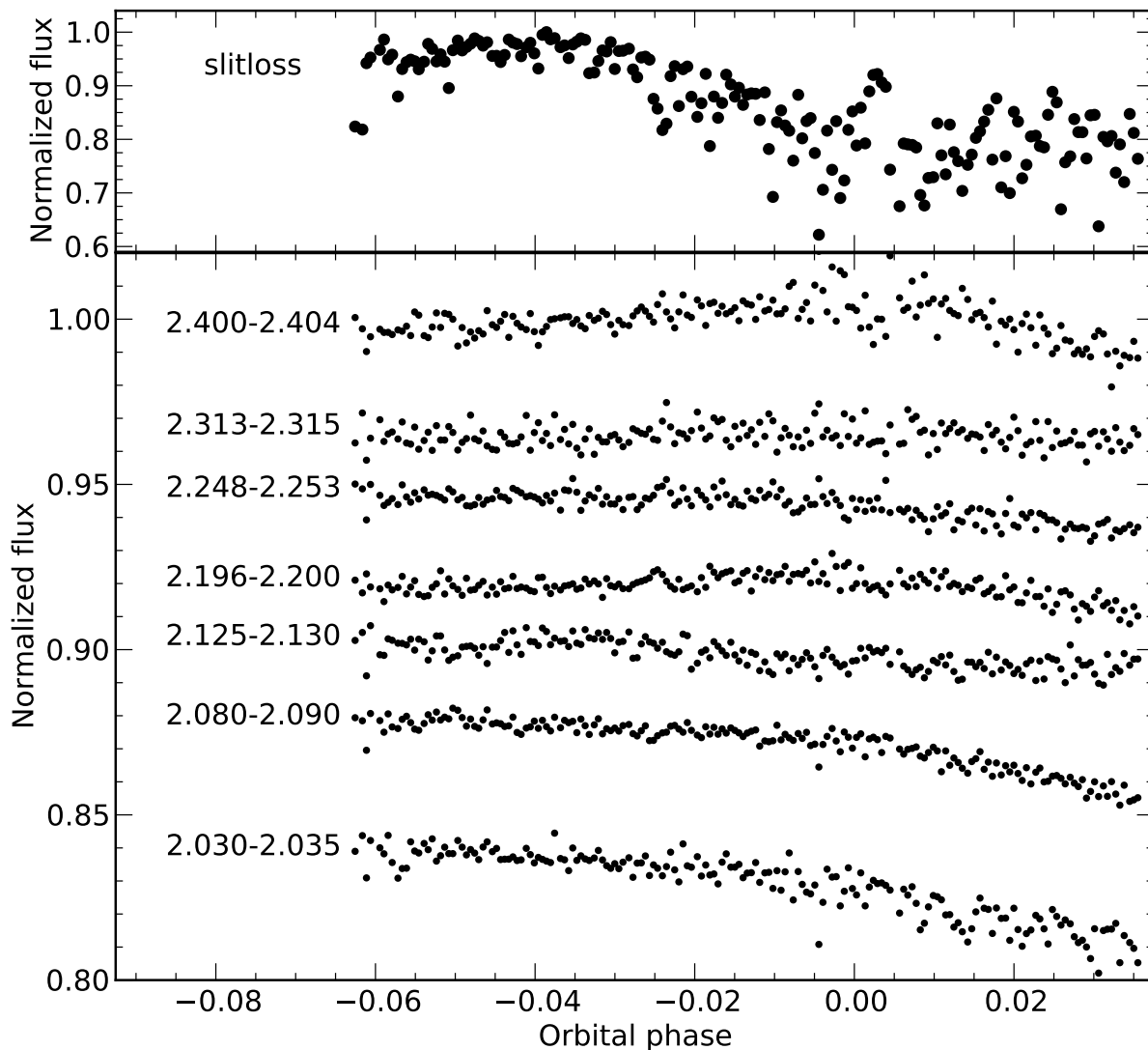


Fig. 5.— Representative spectrophotometric time series. The top panel shows the relative flux coupled into the spectrograph slit, as measured in regions free of telluric absorption lines; telluric continuum absorption and guiding errors combine to produce 10% variations, masking the $\sim 1\%$ transit signature. The bottom panel shows one time series from each echelle order, after removal of the common mode slit loss term and binned over the wavelength range listed (in μm). After correcting for airmass effects these data have variations of order 0.5%, but the transit is still not visible: this is because dividing out the common-mode slit loss term removes a mean transit profile from all the data.

quantity as ℓ and refer to it as the slit loss, though it is actually a combination of instrumental slit losses and telluric continuum absorption due to changing airmass. The slit loss is plotted in Figure 5 with other (cleaned) spectrophotometric time series, and in Figure 6 along with other observable systematics.

High-precision near-infrared photometry demonstrates that apparent photometric variations can be induced by motion of a star across the detector, changes in seeing, and other instrumental sources (e.g.,

Table 3. Telluric-free spectral regions from [Hinkle et al. \(2003\)](#)

Wavelength range (μm)
2.1264290 - 2.1265542
2.1297217 - 2.1299722
2.1304068 - 2.1305100
2.1313866 - 2.1317770
2.1320127 - 2.1322632
2.1326462 - 2.1327346
2.1332503 - 2.1333681
2.1334270 - 2.1336333
2.1344289 - 2.1349077
2.1350624 - 2.1355338
2.1364841 - 2.1367567
2.1370218 - 2.1371176
2.1378911 - 2.1382520
2.1386277 - 2.1388855
2.1390697 - 2.1391655
2.1397769 - 2.1398579
2.1400789 - 2.1409260
2.1410071 - 2.1413459
2.1414859 - 2.1418321
2.1438800 - 2.1439978
2.1798910 - 2.1801862
2.1804436 - 2.1808296
2.1809886 - 2.1824343
2.1856588 - 2.1869077
2.1873467 - 2.1874754
2.1884518 - 2.1885654
2.1886411 - 2.1887849
2.1889590 - 2.1891407
2.1898219 - 2.1902609
2.1907680 - 2.1924106
2.1924938 - 2.1927512
2.1928723 - 2.1940153
2.1940758 - 2.1943105
2.1953777 - 2.1955367
2.1959757 - 2.1961422
2.2077762 - 2.2078973
2.2447114 - 2.2450073
2.3109368 - 2.3111936
2.3125575 - 2.3127902
2.3128624 - 2.3129587
2.3132796 - 2.3134401
2.3138813 - 2.3140418
2.3140980 - 2.3145473
2.3147318 - 2.3148201

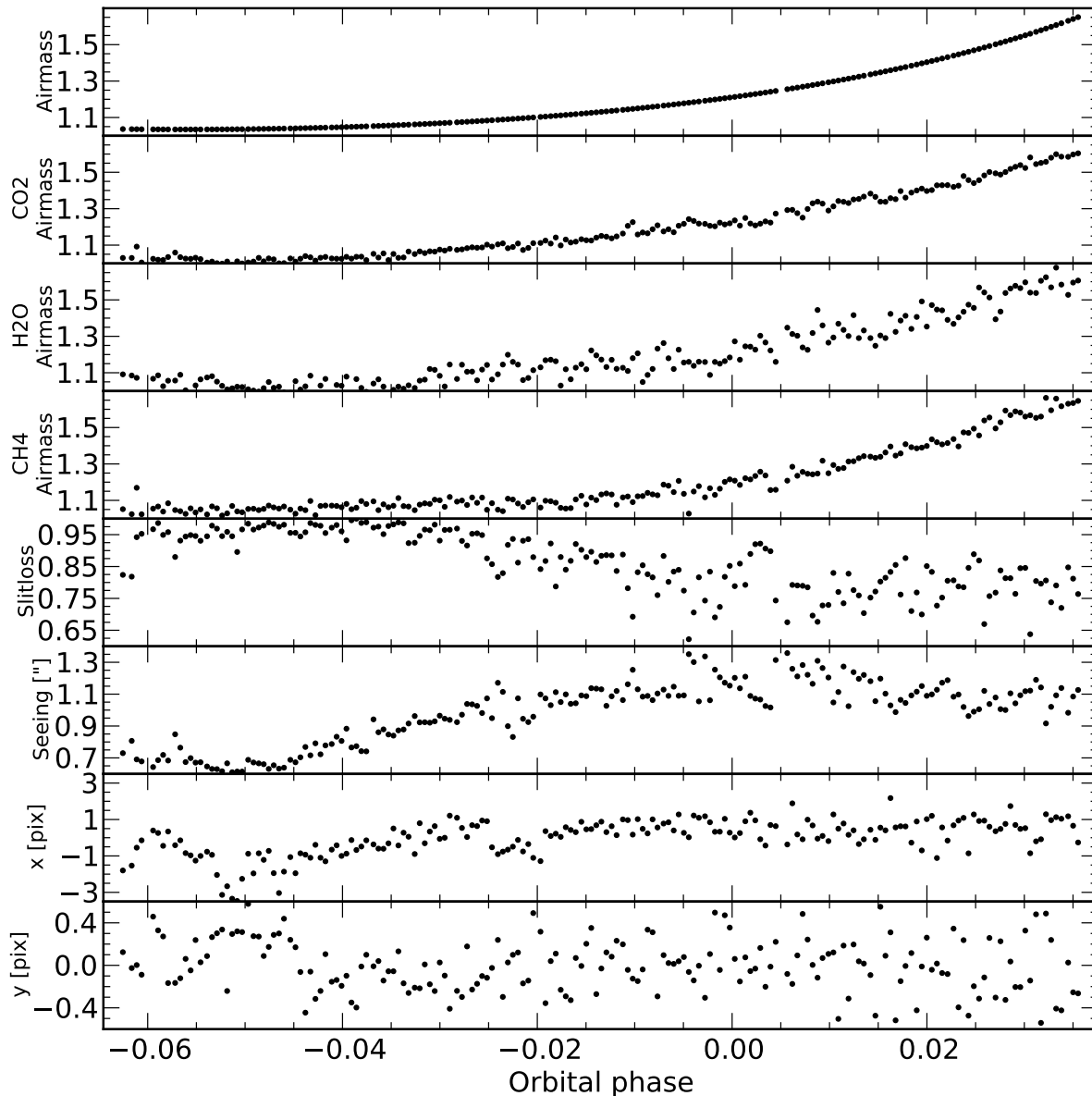


Fig. 6.— The various observable quantities (described in Section 3.2) measured during the course of our observations. As described in the text, we ultimately fit our data using the slitloss term, an empirical airmass quantity derived from the telluric CO₂ line flux, and several low-order polynomials.

Rogers et al. 2009). We expect the same to be true for high-precision spectrophotometry, and so we measure the motion of the spectral profiles in the raw echellograms parallel to (x) and perpendicular to (y) the long axis of the spectrograph slit. We also measure the total amount of light coupled into the spectrograph slit, and the FWHM of the seeing profile. All these quantities are plotted in Figure 6.

We measure the x motion of the spectra on the detector by spline-interpolating the spectrum in each echelle order and cross-correlating it at sub-pixel increments with a high signal to noise (S/N) template spectrum (Deming et al. 2005). We construct our template by taking the temporal average,

after removing outliers, of all our spectra. A parabolic fit to the peak of each spectrum’s cross correlation provides the optimal offset value, and we then spline-interpolate all the spectra to the template’s reference frame.

We measure the y motion of the star along the slit axis by tracing the locations of the spectral profiles using the IRAF `apall` task. The locations of the spectra on the detector are not significantly affected by differential atmospheric refraction, so we use the same set of relative positions for data at all wavelengths. Both x and y motions are plotted in Figure 6; though we see evidence that these motions affect our spectrophotometry (as we discuss in Section 3.4 below), this is a low-amplitude effect.

Though we do not have a measure of the true astronomical seeing during the night, the width of the spectral profiles in the raw echelleograms provides a proxy for seeing. We fit a cubic spline to the mean spectral profile for each echelle order, and measure the average full width at half maximum in each frame. This quantity depends on a combination of astronomical seeing, instrumental focus, and pointing jitter during an exposure, but we hereafter refer to it simply as seeing.

Previous studies (e.g., Deming et al. 2005) report that an empirical measure of atmospheric absorption is preferable to the airmass value calculated from the telescope’s zenith angle when accounting for telluric extinction. To test this, we measure the flux in sets of telluric absorption lines caused by CO_2 , CH_4 , and H_2O . We select these lines, and verify that each is due to only a single absorber, by generating synthetic single-species telluric absorption spectra using the ATRAN code (Lord 1992). We fit the slitloss-corrected flux, f'_i , in these single-species telluric time series to the function $\ln f'_i = p + qa_i$, where a_i is the airmass at timestep i . We then define each species’ empirical airmass term as $a'_i = (\ln f'_i - p) / q$. These different airmass terms are all plotted in Figure 6.

3.4. Identifying and Removing Systematic Effects

After extracting the spectra and quantifying observable systematic effects, our next step is to remove the large-scale flux variations caused by slit losses and (continuum) telluric absorption (note that this is the point in the analysis at which we inject synthetic model transit signals, as discussed later in Section 4.3). We divide the flux in every wavelength channel by the slit loss time series, viz.: $f'_{i\lambda} = f_{i\lambda} / \ell_\lambda$. This improves the S/N in regions clear of telluric absorption lines from $\sim 10 \text{ pixel}^{-1}$ to $\sim 50 \text{ pixel}^{-1}$ (cf. Figures 4 and 7) – this is still > 3 times worse than expected from photon noise. This step removes a mean transit profile from all wavelength channels, but the overall shape of the transmission spectrum should remain the same. We show a set of binned, slitloss-corrected spectrophotometric time series in Figure 5, and show the full set of $f'_{i\lambda}$ in Figure 7.

The most obvious remaining variability is correlated with airmass. We identify other possible sources of variability using Principal Component Analysis (Jolliffe 1986). We compute the strongest several principal components (PCs) in our slit loss-corrected data set, and look for correlations between these PCs and our systematic observables: i.e., x and y motions, seeing, slit losses, sky line emission, and our several airmass proxies. We observe correlations between strong principal components and airmass, x , y , and slit losses, but not with other instrumental parameters. We attribute the x and y dependence to residual flat-field variations as each resolution element moves on the detector. The correlation of slit losses (which have already been removed to first order) with a principal component

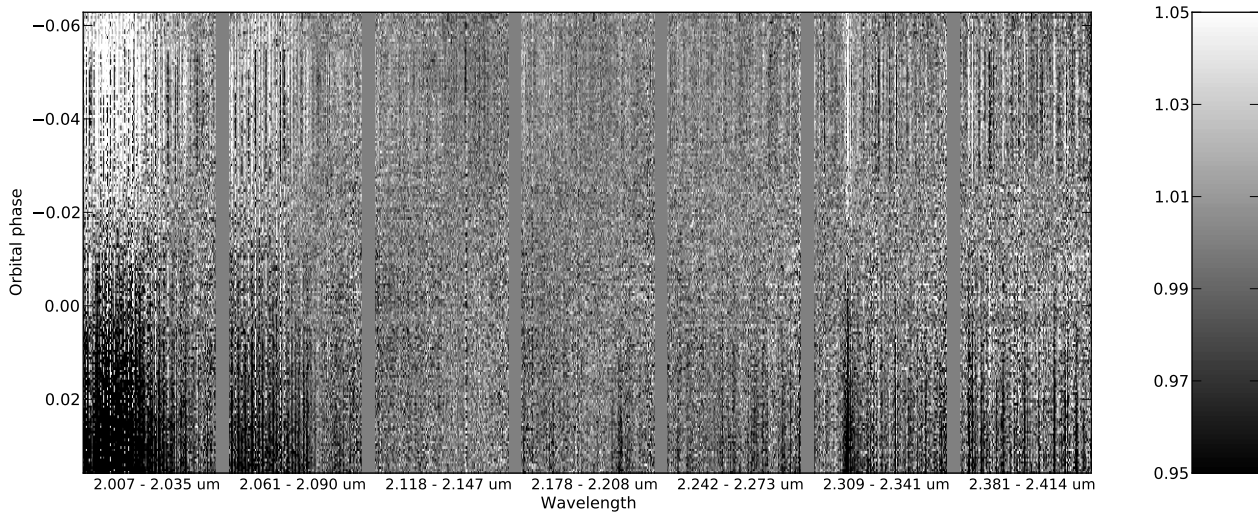


Fig. 7.— Spectrophotometric data $f'_{i\lambda}$ after dividing all wavelength channels by the common mode slit loss term (shown in Figure 5), and normalized by the median value in each wavelength channel. The data shown have variations of order 0.5% after correcting for residual airmass trends, but still no transit is visible because dividing by the slit loss term has removed the mean transit depth from all wavelength channels. For display purposes the the data from each echelle order are separated by a narrow gray region.

which is most prominent in regions of strong telluric absorption suggests flux variations in the core of telluric lines not well explained by a simple exponential extinction relation. As described in Section 4.1, we ultimately detrend our data using only the slit loss term because our precision is not high enough to justify using additional correction terms..

4. Needle in a Haystack: Searching for Transit Signatures

We are unable to measure GJ 1214b’s transit light curve directly, because this signal is buried in the slit loss term we remove from all spectral time series. This removal has the effect of subtracting a constant offset value C from the transmission spectrum. The overall shape of the spectrum is therefore unchanged, and we can still hope to measure the modified transmission spectrum – i.e., $d_\lambda = (R_P/R_*)^2 - C$.

If GJ 1214b has a cloudless, H_2/He -dominated atmosphere we expect substantial variations in d_λ across the wavelength ranges we observe (cf. Figure 2; also Miller-Ricci & Fortney 2010); but if the planet has a denser atmosphere (and thus a smaller atmospheric scale height) we expect to see an essentially flat transit spectrum – in this case we might see no transit signature in any wavelength channel. Clouds would further suppress any spectral features occurring below a given altitude.

Photon noise alone precludes detection of the residual differential transit signal in any single spectral line. Even when examining time series that average over broad spectral regions (e.g., molecular bandheads) we are unable to detect any transit-like features. This agrees with our conclusion that, at our sensitivity, the spectrum is consistent with being featureless. To achieve our final sensitivity we must use our entire wavelength coverage. Our data do not permit us to search for any individual spectral

features (cf. Redfield et al. 2008), but they do allow us to test a given model against the entirety of our data.

Note that we cannot use exactly the same cross-correlation technique successfully used by Snellen et al. (2010) in their detection of CO on HD 189733b. This is because (a) GJ 1214b exhibits a much smaller change in velocity during a transit than does HD 189733b, (b) our spectral resolution is much lower (17,000 with NIRSPEC vs. 100,000 with CRIFES), and (c) the signal to noise of our (fewer) spectra are substantially lower. For similar reasons, and because the most optimistic models of planetary emission predict planet-to-star contrast ratios of $\lesssim 10^{-4}$ for GJ 1214b, we cannot use the spectral deconvolution techniques used by Barnes et al. (2010) to search for planetary emission.

Instead, we search for residual transit signatures in our data by fitting a model (including telluric, systematic, and transit effects) to the time series in each wavelength channel, as described in Section 4.1. We then compare the extracted transmission spectrum to model spectra using both cross-correlation and linear least squares techniques, as described in Section 4.2.

4.1. Fitting the data

We fit each spectral time series (i.e., the slitloss-corrected flux in each wavelength bin) with the following relation:

$$f'_{i\lambda} = f_{0\lambda} e^{b_\lambda a_i} (1 + d_\lambda r_i) \left(1 + \sum_{j=1}^J c_{j\lambda} v_{ji} \right) \quad (1)$$

This equation represents a transit light curve affected by systematic and telluric effects. In all cases the subscript i refers to the frame number and λ to the particular wavelength bin. The variables are: $f'_{i\lambda}$, the slitloss-corrected measured flux; $f_{0\lambda}$, the out-of-transit flux that would be measured above the Earth’s atmosphere; r_i , the flux in a transit light curve scaled to equal zero out of transit and approximately -1 inside transit (i.e., $(F - 1)/(R_P/R_*)^2$, using the nomenclature of Mandel & Agol 2002); d_λ , the depth of transit; v_{ij} , the J state vectors expected to have a linearly perturbative effect on the instrumental sensitivity; $c_{j\lambda}$, the coefficients for each state vector; and a_i , the airmass, which has an exponential extinction effect on the measured flux modulated by an extinction coefficient b_λ . Since residual, low-amplitude drifts are common in this kind of observation (cf. Swain et al. 2010; Bean et al. 2010) we account for and remove the effect of these drifts by including a series of low-order Chebychev polynomials in orbital phase in the set of vectors v_{ji} . After fitting we obtain a set of coefficients ($f_{0\lambda}, b_\lambda, c_{j\lambda}, d_\lambda$) from our full set of observations; the d_λ represent our measured transmission spectrum.

We use the parameters of Carter et al. (2010) for our model transit light curve and use a nonlinear limb-darkened light curve using the small-planet approximation from Mandel & Agol (2002). We take our near-infrared limb-darkening coefficients from Claret (2000) for a star with $T = 3000$ K and surface gravity 10^5 cm s^{-1} . In any case we are not especially sensitive to different limb-darkening models – even a uniform-disk transit curve leaves our results unchanged within their uncertainties.

We initially fit our data using many combinations of state vectors and low-order polynomials, and

both calculated and empirical airmass quantities. We use the Bayesian Information Criterion³ (BIC) to choose which of these many parameter sets best fit our data. Calculating the BIC involves computing χ^2 from each set of parameters, which in turn requires us to assign uncertainties to each datapoint. We estimate these uncertainties as follows. We first compute unweighted fits of Eq. 1 (using no v_{ji} , and airmass as reported from the telescope control system) to the data using a multivariate minimization provided in the SciPy⁴ software distribution (the function `optimize.leastsq`), and compute the residuals for each time series. We then assign uncertainties to the individual datapoints by adding in quadrature the expected photon noise and the standard deviation of the residuals in each time series, and then globally scale all uncertainties in each wavelength channel to give a χ^2 equal to the number of datapoints. We then use these scaled values as our per-point measurement uncertainties. Although this method of estimating uncertainties is not statistically valid inasmuch as it overestimates our goodness-of-fit (especially considering that near-infrared photometry typically only comes within a factor of 5 of the photon noise limit) and underestimates parameter uncertainties (Andrae 2010), it provides a quantitative measure with which to compare the relative merit of various models.

The instrumental model which gives the lowest global BIC for our data include polynomials up to cubic order, the slit loss term described previously, and an empirical airmass calculated from the sum of flux in unsaturated telluric CO₂ lines from 2.0 – 2.1 μm . We confirmed that this result is not dominated by the first two echelle orders (populated with the numerous telluric CO₂ lines from which we construct our empirical CO₂ airmass) by excluding these orders and repeating the BIC analysis; the same set of parameters still deliver the lowest BIC.

The relative transit depth spectrum d_λ that results from the fitting process represents a modified transmission spectrum of GJ 1214b; specifically, $d_\lambda = (R_P(\lambda)/R_*)^2 - C$. The constant C is the mean transit depth removed by our correction for slit loss variability. For display purposes, we show our extracted spectrum – averaged in wavelength – in Figure 8; note that we do not fit to the binned data shown there. Regions of strong telluric absorption (especially for $\lambda < 2.1 \mu\text{m}$) are notably biased, and we see a distinct tilt in all echelle orders. We suspect (but cannot independently confirm) that this tilt is some sort of detector artifact; we also see it in the spectra we extract after injecting model spectra into our data (cf. Section 4.3). We do not know the origin of this intra-order slope. Removing this tilt from each order does not markedly increase our sensitivity, and to be conservative we do not remove it from our data. Our sensitivity tests demonstrate that we are still sensitive to plausible injected models in the presence of this slope.

We assess σ_{d_λ} , the uncertainties on d_λ , in two ways: using the residual permutation (“prayer-bead”) method (Gillon et al. 2007), and by quantifying how our extracted parameters vary as we inject model transits at different times. The residual permutation technique fits fake datasets that are generated by adding temporally shifted copies of the residuals to the best-fit model. Thus it is similar to the bootstrap method, but has the advantage of preserving the properties of correlated noise (present in our data). We estimate the 68.3% confidence interval on the d_λ by marginalizing over all other parameters and determining the parameter values that enclose the central 68.3% of the resulting one-dimensional

³Bayesian Information Criterion (BIC) = $\chi^2 + k \ln N$, where k is the number of free parameters and N the number of datapoints.

⁴Available at <http://www.scipy.org/>.

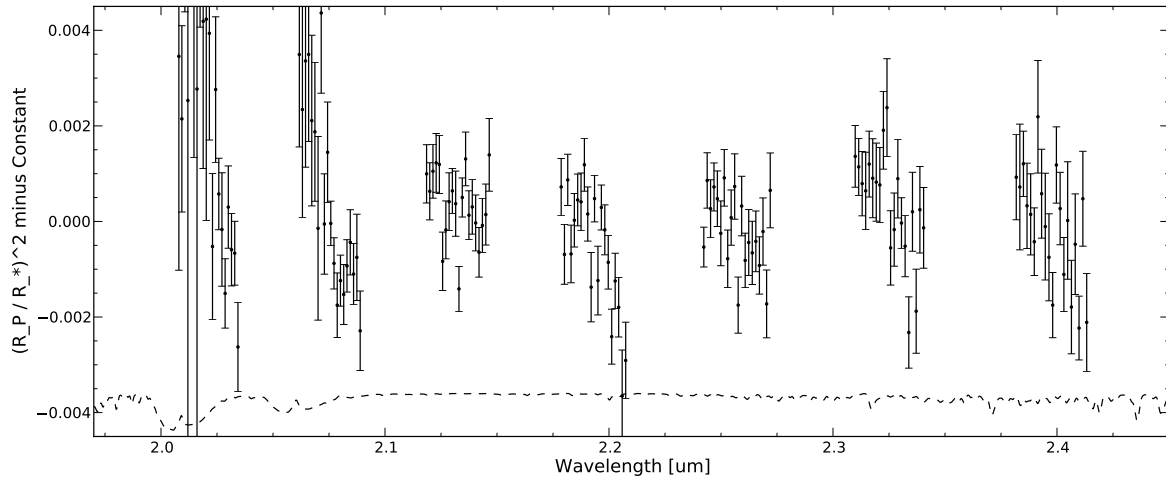


Fig. 8.— Extracted transmission spectrum of GJ 1214b, binned to 1.5 nm for display purposes; error bars here represent solely statistical (standard deviation on the mean) errors. Regions of strong telluric absorption (e.g., shortward of 2.1 μm) are notably biased. We do not know the source of the tilt in each echelle order. The dashed line at bottom represents the telluric transmission from [Hinkle et al. \(2003\)](#).

parameter distributions.

Our second technique to determine parameter uncertainties injects model transit spectra into our dataset (as described in Section 4.3) with varying ephemerides. We vary the injected transit ephemeris from 90 minutes before to 45 minutes after the expected time of transit, and we observe how the extracted transmission spectrum varies. These variations demonstrate the extent to which temporal evolution of systematic effects may limit our sensitivity.

We find that the σ_{d_λ} computed through this second technique are generally larger than the uncertainties from our residual-permutation analysis. To be conservative we assign the differential transit depth in each wavelength channel an uncertainty equal to the larger of the uncertainties from the two techniques.

4.2. Comparing models to data

We compare d_λ , the extracted transmission spectrum, to the spectral transmission models described in Section 2.2 in two ways. First, we cross-correlate our extracted spectrum with each model and measure the integrated signal centered at zero lag. Second, we fit our extracted spectrum to (a) each model spectrum and (b) a flat, featureless spectrum (representing a nondetection) and compare the BIC of each fit.

We require that a robust detection of a given model must satisfy several criteria. First, we require that d_λ is better fit by the tested model than by a flat spectrum. Second, we require that the integrated cross-correlation signal (i) is consistent with what we see when injecting synthetic models into our data and (ii) is significantly greater than zero. If a particular model meets these criteria with the injected signals but not with the unadulterated, observed data then we rule out the model as a plausible

description of GJ 1214b’s atmosphere. A model is unconstrained if we are unable to reliably recover it when it has been injected into the data. Since we ultimately achieve no positive detections, our main result is our ability to rule out a large segment of atmospheric parameter space.

We do not use the entire set of extracted d_λ when comparing to models. We exclude wavelength channels with $S/N < 40$, which mainly affects spectral regions of low telluric or instrumental transmission. We also exclude all data from the first two echelle orders ($\lambda < 2.1\mu\text{m}$), because these wavelengths are heavily corrupted by numerous, strongly saturated absorption features from telluric CO_2 . Finally, we exclude the region $2.196\mu\text{m} < \lambda < 2.2\mu\text{m}$ because those portions of the data are visibly corrupted by detector anomalies. In all cases we use $\sim 4,200$ (out of 7,168 possible) $\sim 0.3 \text{ \AA}$ wavelength channels in the tests that follow.

4.2.1. Template cross-correlation

We first compare our extracted transmission spectrum, d_λ , against atmospheric models by cross-correlating with the model spectra described in Section 2.2. We investigated the use of the Least-Squares Deconvolution algorithm (Donati et al. 1997; Barnes et al. 2007) to compare our measured transmission spectrum with model spectra, but we find this method to be less sensitive than straightforward cross-correlation.

Instead, we use the Discrete Correlation Function (DCF; Edelson & Krolik 1988) to perform a cross-correlation between d_λ and each spectral model. The DCF has several advantages over standard (linear-shift) methods for computing cross-correlations: it obviates the need for interpolation to a linear wavelength grid, and it allows us to compute the cross-correlation while excluding low S/N channels without the need for interpolating across the resulting gaps. In the case of regularly sampled data the DCF gives results identical to linear-shift cross-correlation.

For each model transmission spectrum, we cross-correlate our extracted transmission spectrum with the model over each echelle order. We then take the weighted average of these several cross-correlations, where the weights are proportional to the number of wavelength channels used to compute each echelle order’s DCF.

In the limit of high S/N and perfect correspondence between our model and the observed transmission spectrum this analysis is equivalent to computing the transmission spectrum autocorrelation. We show the autocorrelation for each echelle order, and the weighted average, in Figure 9 for the case of our solar abundance model. The mean autocorrelation shows features on two characteristic scales: a strong, narrow (tens of km s^{-1}) peak and a much broader ($\sim 200 \text{ km s}^{-1}$) plateau of lower amplitude; we refer to these as the narrowband and broadband cross-correlation signals, respectively. The former results mainly from the individual, narrow spectral features while the latter results from broader variations of transit depth with wavelength. Integrating over these two correlation lag scales provides us with two measures of the cross-correlation signal, which we denote $\sum\text{DCF}$. By varying the range of summation we determined that we achieve the highest S/N with summation limits set at $|v_{lag}| \leq 10 \text{ km s}^{-1}$ and $|v_{lag}| \leq 200 \text{ km s}^{-1}$.

Examples of this cross-correlation process are shown in Figures 10-14 for several of our models.

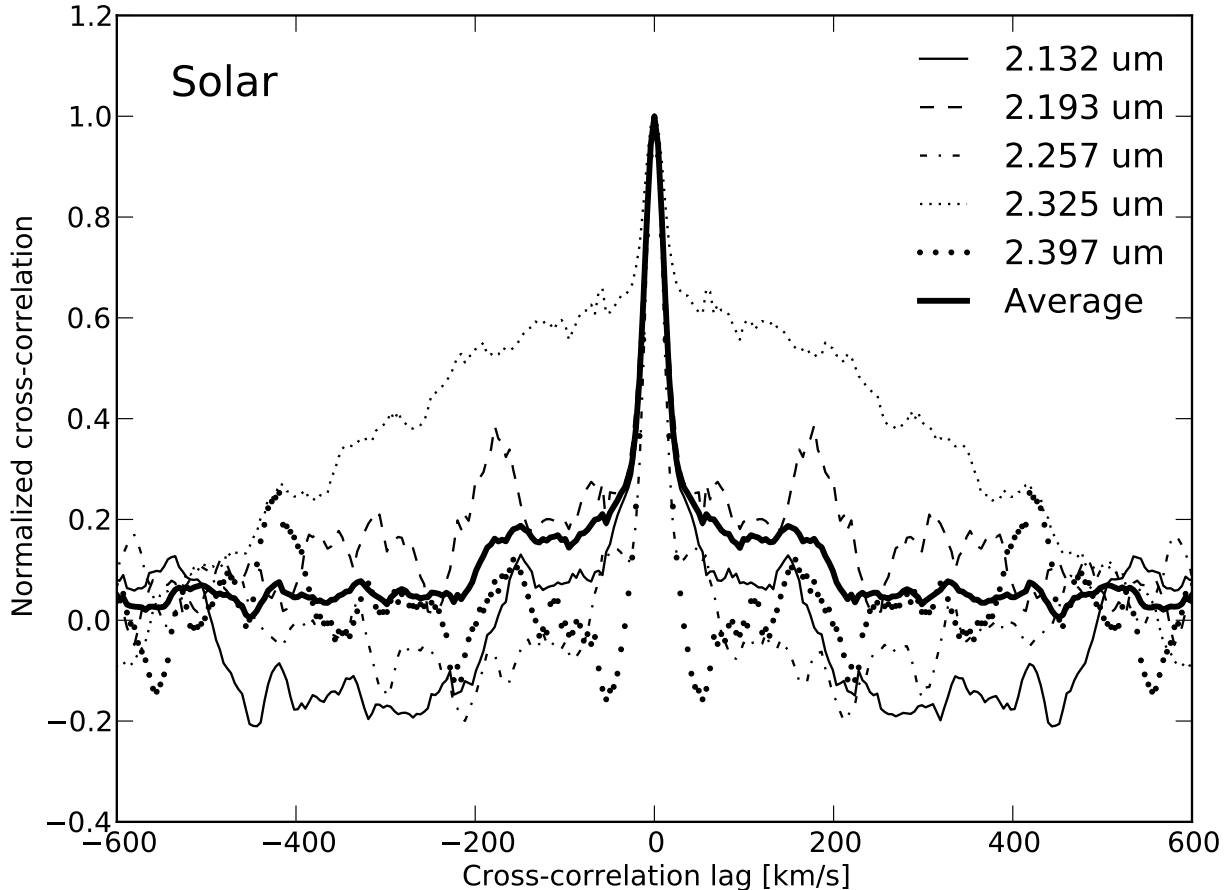


Fig. 9.— Autocorrelation of our solar abundance model computed in each echelle order (thin lines), and the average (thick solid line) weighted by the number of wavelength channels used in our analysis. All orders show a strong, narrow peak resulting from the narrow features in the model; broader structures (e.g. in the $2.325 \mu\text{m}$ order) result from broad spectral variations (cf. Figure 3). In the limit of infinite S/N, this figure shows our expected cross-correlation signal.

These cross-correlations do not closely resemble the noiseless autocorrelation shown in Figure 9 because of residual instrumental and telluric sources of measurement error. We verified that, on average, the expectation value for the effect of our noise sources on the cross-correlation values is zero and thus the expectation values for our integrated signals are unaffected.

We quantify the significance of a $\sum\text{DCF}$ measurement as follows. We set our measurement uncertainty by taking the standard deviation of the $\sum\text{DCF}$ values measured at alternate transit ephemerides (and thus in the absence of any exoplanetary signal). We also simulated cross-correlation functions by resampling a smoothed fit to the mean power spectrum of the measured cross-correlation functions, and then examining the frequency with which peaks of a particular amplitude occur in this simulated data; these two techniques give comparable results, which give us confidence in our measurement uncertainty. We then estimate the expected $\sum\text{DCF}$ value in the presence of a known signal by injecting

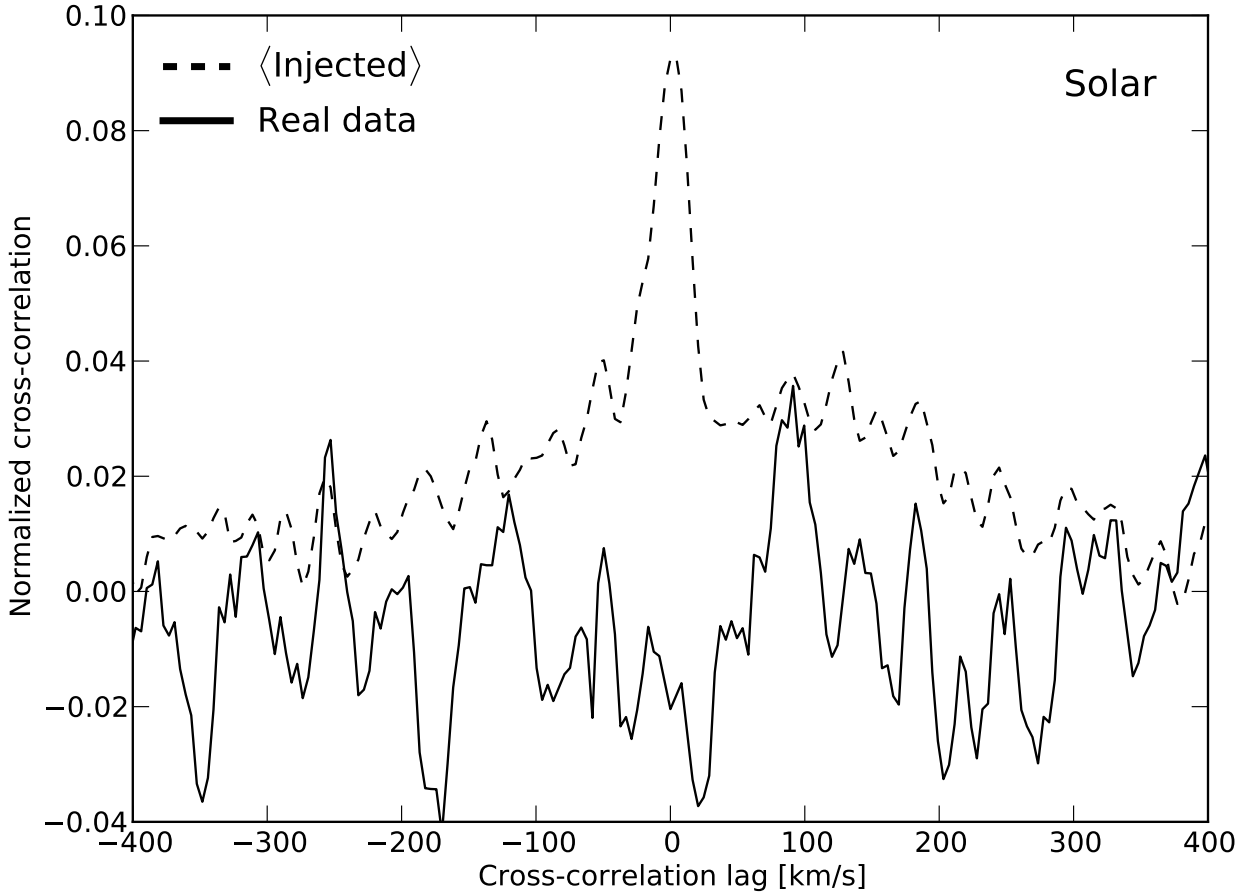


Fig. 10.— Template cross-correlation results. The solid line is the Discrete Correlation Function (DCF) of our solar-composition model with our extracted, unbinned transmission spectrum. The dashed line is the mean extracted DCF of the same model with data into which the transit signature of the model has been injected (cf. Section 4.3). The integrated signal over our narrowband ($|v_{lag}| \leq 10 \text{ km s}^{-1}$) and broadband ($|v_{lag}| \leq 200 \text{ km s}^{-1}$) apertures differ from the mean injected signal by 4.6σ and 5.6σ , respectively. This allows us to rule out this model as a good representation of the transmission spectrum of GJ 1214b.

and re-extracting models into our data at varying ephemerides (as described in Section 4.3). We take the mean and standard error on the mean of the $\sum \text{DCF}_{inj}$ to be our best estimate of this quantity. We list all these values in Table 4. The agreement between the injected ($\sum \text{DCF}_{inj}$) and nominal ($\sum \text{DCF}_0$) values indicates the degree to which the model corresponds to our measurements; if they disagree at $> 3\sigma$ we rule out the model being tested. Detection of a model would require the two cross-correlation sums to be consistent and $\sum \text{DCF}_0$ to be significantly greater than zero.

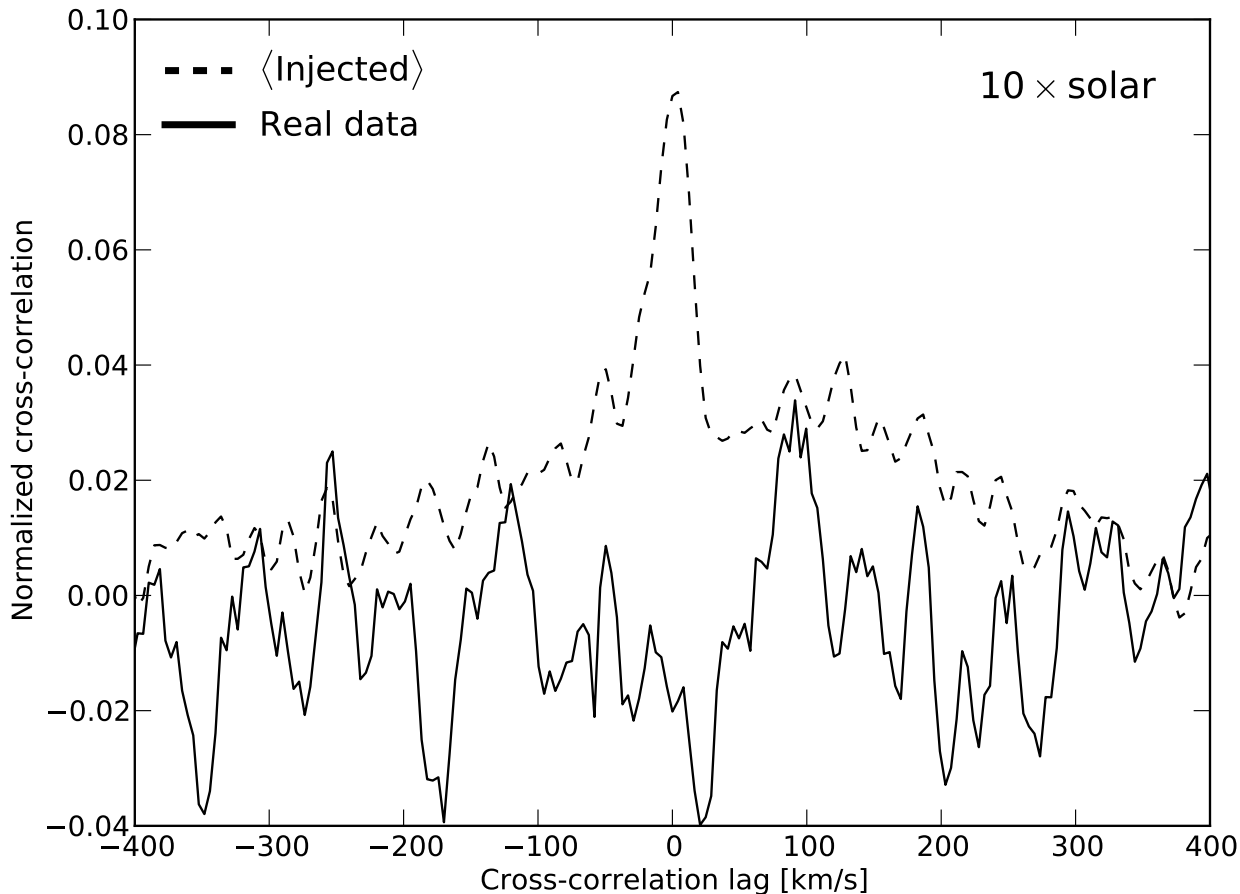


Fig. 11.— Same as Figure 10, but for our $10\times$ solar abundance model. The narrowband and broadband integrated signals differ from the mean injected signal by 4.4σ and 5.4σ , respectively. This allows us to rule out this model as a good representation of the transmission spectrum of GJ 1214b.

4.2.2. Least-squares template matching

We also compare the extracted spectrum, d_λ , to the various spectral models using weighted linear least squares. We determine the offset value C necessary to give the best match between the measured and model spectra using $1/\sigma_{d_\lambda}^2$ as the weights – that is, we solve $d_\lambda = m_\lambda - C$ in a least squares sense, where m_λ is the model spectrum being tested. The offset C results from our removal of the absolute transit depth by our correction for slit losses. We compute the statistic ΔBIC equal to the difference between the BIC for each model and the BIC resulting from a flat, featureless spectrum (i.e., a nondetection). Then, $\Delta\text{BIC} \leq 0$ implies the data are more consistent with a constant $R_P(\lambda)$ than with the tested atmospheric model, while $\Delta\text{BIC} > 0$ indicates we are justified in preferring the additional parameter – i.e., the model spectrum – to match our data. We list the ΔBIC from comparing each of our spectral models in Table 4.

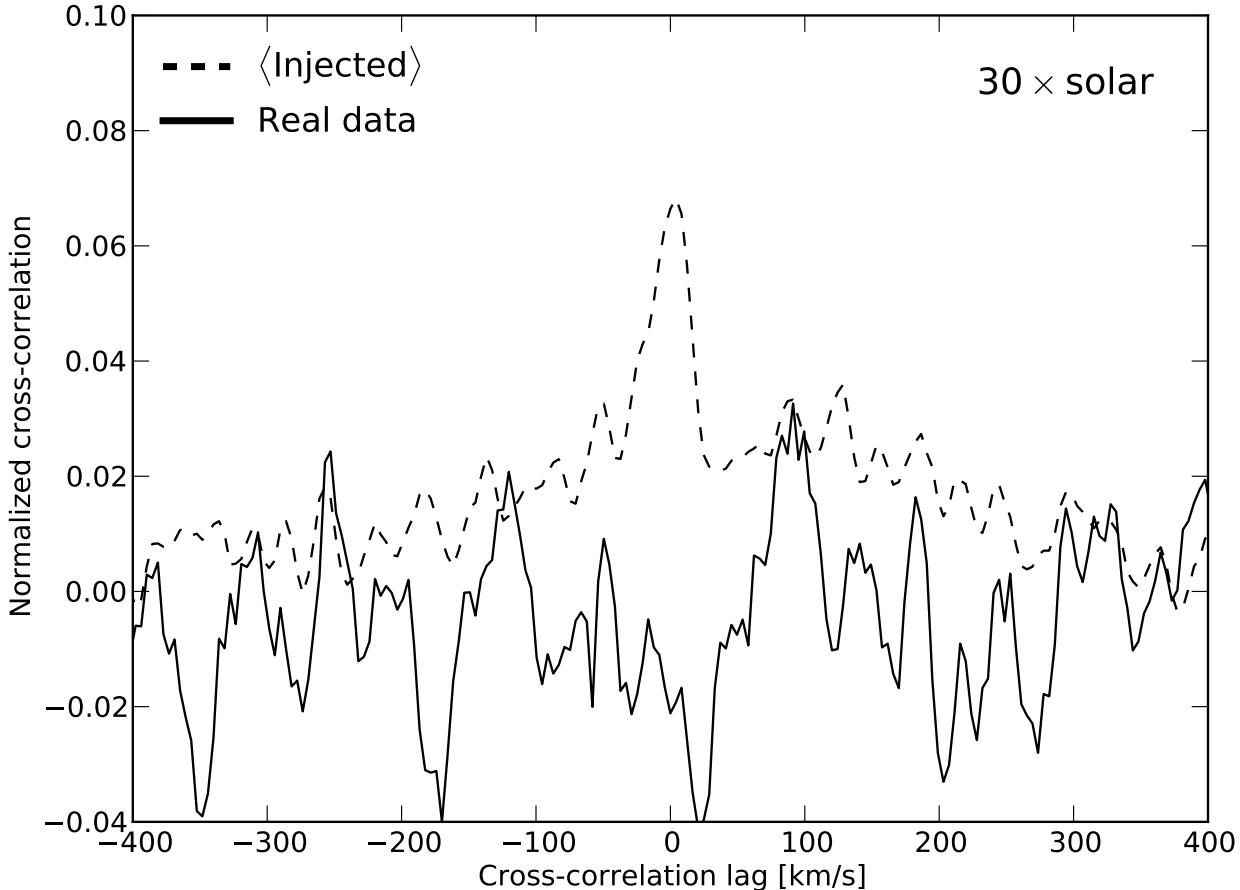


Fig. 12.— Same as Figure 10, but for our $30\times$ solar abundance model. The narrowband and broadband integrated signals differ from the mean injected signal by 3.6σ and 4.7σ , respectively. This allows us to rule out this model as a good representation of the transmission spectrum of GJ 1214b.

4.3. Sensitivity tests: injected models

As previously alluded to, we test the sensitivity of our analysis by inserting our model transmission spectra (cf. Section 2.2) into our extracted echelle spectra and attempting to recover the injected signal. We include both the time-dependent wavelength shift of the transmission spectrum due to the planet’s orbital motion and the overall transit light curve shape in each wavelength channel. All data outside of the simulated transit are unaffected. We inject these signals using ephemerides shifted by up to 90 minutes earlier than, and 45 minutes later than, the true transit ephemeris at intervals of 15 minutes. We inject each model spectrum immediately before the echelle spectra have been brought to a common wavelength frame (i.e., at the beginning of Section 3.4) and repeat the same analyses and tests as described in the preceding sections. The mean and error on the mean of the ensemble of the results of these injected and re-extracted spectra are listed in Table 4; these define our sensitivity limits.

Table 4. Results from spectral model testing

Model	σ_{R_P} ^a			$ v_{\text{lag}} \leq 10 \text{ km s}^{-1}$		$ v_{\text{lag}} \leq 200 \text{ km s}^{-1}$		Result ^e
		ΔBIC_0 ^b	$\langle \Delta\text{BIC}_{\text{inj}} \rangle$ ^b	$\sum_v \text{DCF}_0$ ^c	$\langle \sum_v \text{DCF}_{\text{inj}} \rangle$ ^d	$\sum_v \text{DCF}_0$ ^c	$\langle \sum_v \text{DCF}_{\text{inj}} \rangle$ ^d	
30× solar	0.058	-180	177	-0.35(43)	1.33(17)	-2.0(2.4)	10.2(1.0)	Ruled out
" ($\log_{10}(\text{CH}_4) \sim -3.0$)	0.052	-150	148	-0.35(43)	1.20(16)	-2.0(2.4)	9.4(1.0)	Ruled out
" ($\log_{10}(\text{CH}_4) \sim -4.0$)	0.047	-124	122	-0.34(43)	1.07(16)	-1.9(2.5)	8.7(1.0)	Ruled out
" ($\log_{10}(\text{CH}_4) \sim -5.1$)	0.041	-101	99	-0.34(43)	0.95(16)	-1.7(2.5)	7.9(1.0)	Unconstrained
10× solar	0.076	-288	285	-0.33(43)	1.70(17)	-2.1(2.5)	12.5(1.1)	Ruled out
" ($R_{\text{min}} = 2.85 R_{\oplus}$)	0.071	-255	234	-0.37(44)	1.58(18)	-2.5(2.7)	11.8(1.2)	Ruled out
" ($R_{\text{min}} = 2.9 R_{\oplus}$)	0.064	-205	176	-0.44(47)	1.39(19)	-3.1(2.8)	10.7(1.2)	Ruled out
" ($\log_{10}(\text{CH}_4) \sim -3.6$)	0.069	-238	237	-0.33(43)	1.54(17)	-2.0(2.5)	11.5(1.1)	Ruled out
" ($\log_{10}(\text{CH}_4) \sim -4.6$)	0.061	-194	194	-0.32(43)	1.37(17)	-1.9(2.6)	10.5(1.1)	Ruled out
" ($\log_{10}(\text{CH}_4) \sim -5.6$)	0.054	-155	156	-0.31(43)	1.21(16)	-1.8(2.6)	9.5(1.1)	Ruled out
" ($\log_{10}(\text{CH}_4) \sim -6.6$)	0.047	-122	122	-0.30(43)	1.05(16)	-1.6(2.7)	8.4(1.1)	Unconstrained
Solar	0.082	-329	315	-0.34(43)	1.81(18)	-2.4(2.5)	13.1(1.1)	Ruled out
" ($R_{\text{min}} = 2.85 R_{\oplus}$)	0.081	-320	300	-0.34(43)	1.78(18)	-2.5(2.6)	12.9(1.1)	Ruled out
" ($R_{\text{min}} = 2.9 R_{\oplus}$)	0.075	-291	193	-0.39(45)	1.46(19)	-2.9(2.7)	10.8(1.4)	Ruled out
" ($\log_{10}(\text{CH}_4) \sim -3.8$)	0.074	-273	263	-0.33(43)	1.63(18)	-2.4(2.6)	12.1(1.1)	Ruled out
" ($\log_{10}(\text{CH}_4) \sim -4.7$)	0.067	-224	216	-0.33(43)	1.45(17)	-2.3(2.6)	11.0(1.1)	Ruled out
" ($\log_{10}(\text{CH}_4) \sim -5.5$)	0.059	-179	174	-0.32(43)	1.28(17)	-2.3(2.7)	9.9(1.1)	Ruled out
" ($\log_{10}(\text{CH}_4) \sim -6.4$)	0.052	-141	137	-0.31(43)	1.10(17)	-2.2(2.7)	8.8(1.1)	Ruled out
" ($\log_{10}(\text{CH}_4) \sim -7.3$)	0.045	-107	104	-0.30(43)	0.93(16)	-2.0(2.8)	7.7(1.1)	Unconstrained
" (low carbon)	0.050	-61	36	0.20(34)	0.99(13)	-1.5(1.7)	2.6(0.6)	Unconstrained
" (low C; $v_0 = 20 \text{ km s}^{-1}$) ^f	0.050	-61	36	0.72(38)	0.99(13)	-1.6(1.6)	2.6(0.6)	Unconstrained
" (no methane)	0.026	-14	6.1	0.22(49)	0.35(17)	2.1(3.1)	0.1(0.1)	Unconstrained

^aStandard deviation of the model $R_P(\lambda)$, in Earth radii, over the wavelengths used in our analysis and at our model resolution.

^b $\Delta\text{BIC} = \text{BIC}_{\text{flat}} - \text{BIC}_{\text{model}}$; a positive value implies that the the extracted transmission spectrum is better fit by the given spectral model than by a flat, featureless spectrum; cf. Section 4.

^cCross-correlation sum for the nominal case – i.e., the true transit ephemeris and without any injected signal. The uncertainty quoted is the standard deviation of the quantities measured at alternate transit ephemerides.

^dExpectation value in the case of a positive signal, estimated by calculating the mean and standard deviation on the mean of the values measured for the injected cases.

^eTo rule out a model we require that $\Delta\text{BIC} > 0$ in the injected case and that $\sum_v \text{DCF}_0 < \langle \sum_v \text{DCF}_{\text{inj}} \rangle$ at greater than 3σ confidence for both the narrowband and broadband cross-correlation signals.

^fLow carbon model, but with the limits of cross-correlation integration shifted by 20 km s^{-1} to encompass the feature centered there (cf. Figure 14). The model is still unconstrained in this case because the narrowband $\sum \text{DCF}_0$ is still $< 2\sigma$ discrepant from zero.

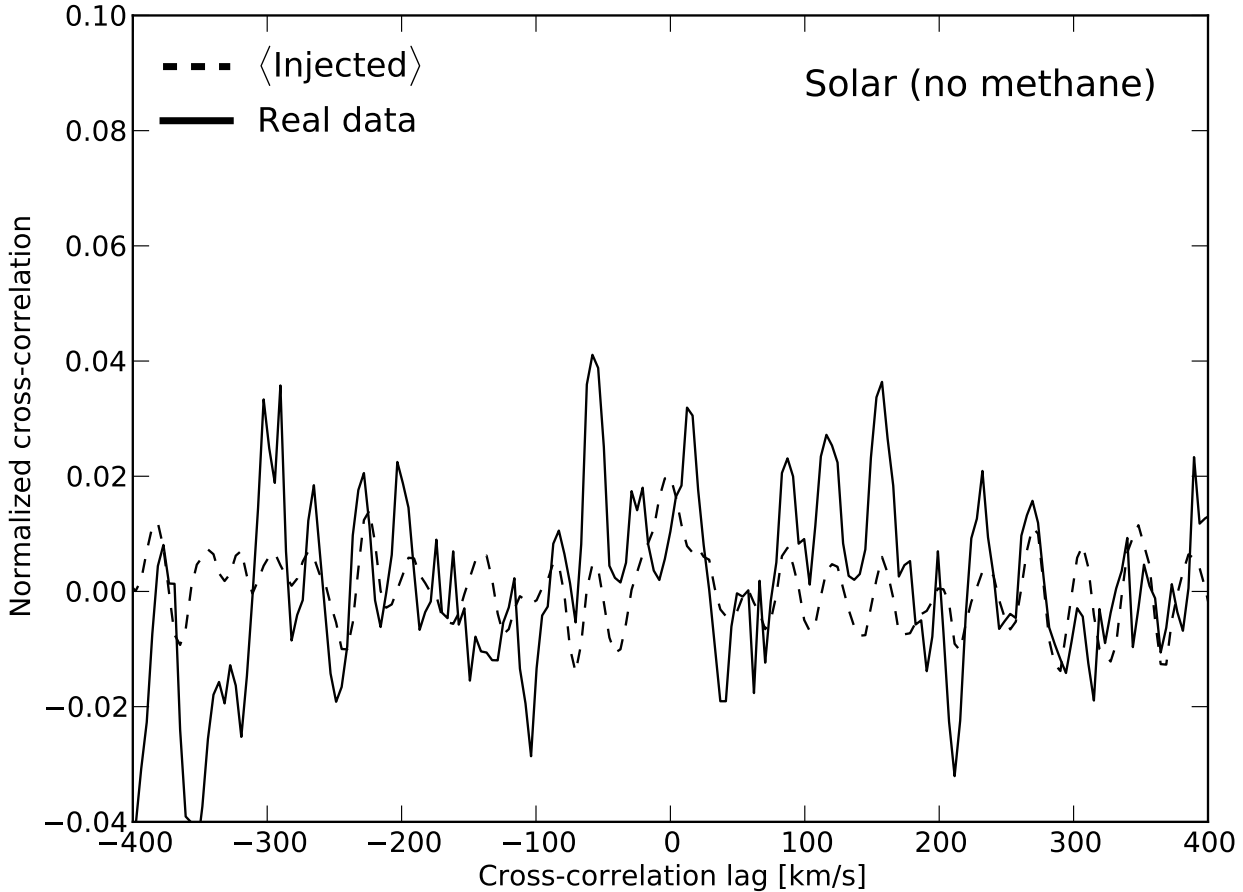


Fig. 13.— Same as Figure 10, but for our solar abundance, methane-free model. This model is quite flat and so we barely see a cross-correlation signal in the average, injected case; therefore our sensitivity does not allow us to state with confidence whether such a model represents the transmission spectrum of GJ 1214b.

5. Results and Discussion

5.1. Spectroscopic results

We see no evidence of a significant match between our extracted transmission spectrum and any of our various spectral models. These nondetections are significant because our sensitivity analysis described above demonstrates our ability to recover signals of comparable magnitude in our data, as demonstrated by the values of ΔBIC and $\sum\text{DCF}$ listed in Table 4 for each model. In this section we discuss the results of our spectroscopic analysis, and in the section that follows we discuss these results in the context of other observations.

We rule out cloud-free atmospheres in chemical equilibrium with solar, $10\times$ solar, and $30\times$ solar abundances. Additionally, we rule out clear atmospheres with CH_4 abundances reduced from that expected in chemical equilibrium: we constrain $\log_{10}(N_{\text{CH}_4})$, the CH_4 molar abundance, to be < -6.4 , $<$

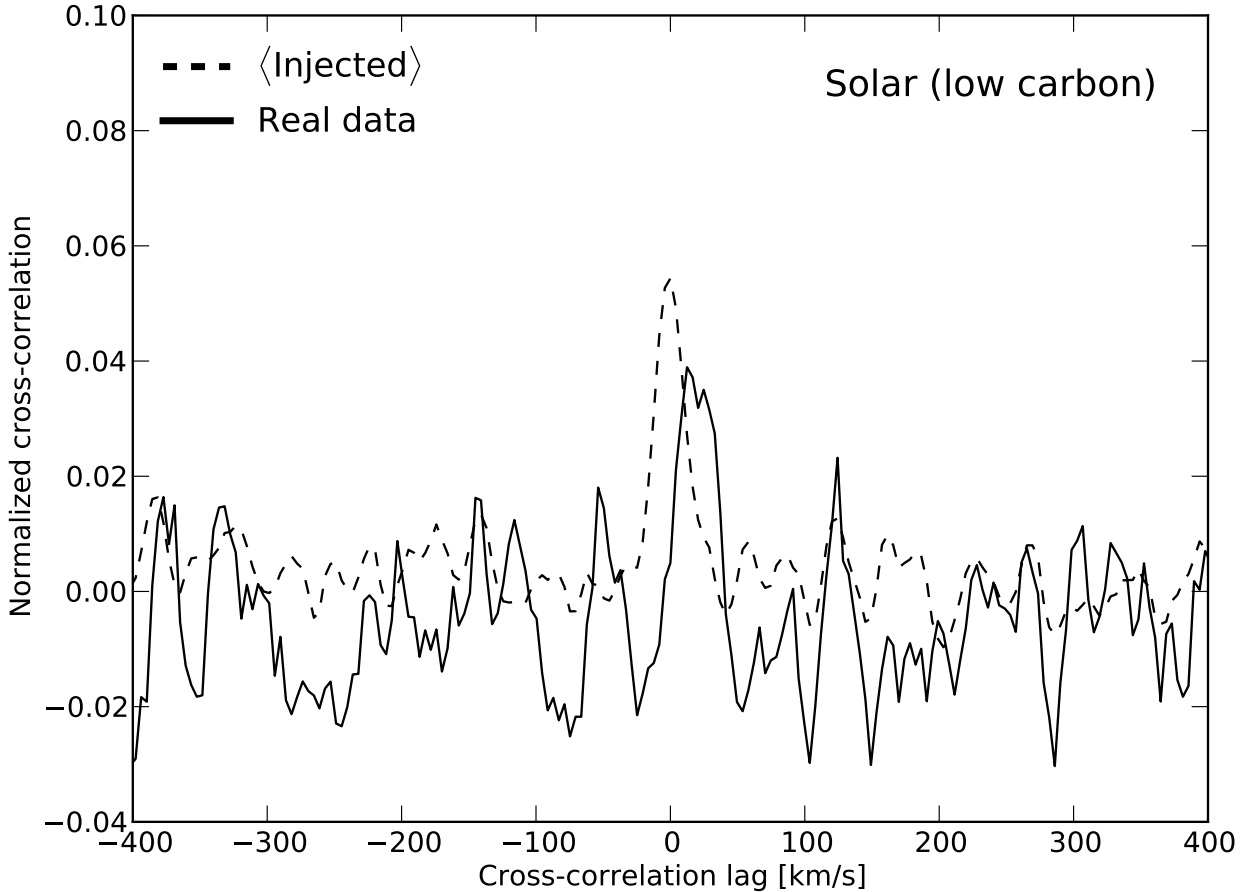


Fig. 14.— Same as Figure 10, but for our low carbon abundance solar model. The intriguing signal at $v \sim 20 \text{ km s}^{-1}$ has approximately the right shape and size as the expected signal but represents only a 1.9σ detection; in addition its offset from zero lag seems too large to result from uncertainties in either GJ 1214b’s orbit or in our wavelength calibration. We deem this feature a false positive, and otherwise our sensitivity does not allow us to state with confidence whether such a model represents the transmission spectrum of GJ 1214b.

5.6, and < 4.0 in the case of solar, $10\times$ solar, and $30\times$ solar abundance, respectively. In general we have less ability to discriminate between variants of the $30\times$ solar model than of the solar abundance model. This is because the variations of transit depth with wavelength decrease with increasing atmospheric metallicity, as seen in Figure 3, because a greater mean molecular weight results in a smaller scale height and thus a general suppression of the amplitudes of all spectral features. A similar trend is also apparent in the models of Miller-Ricci & Fortney (2010) with atmospheres even more enriched in heavy elements. We demonstrate an ability to constrain the presence of clouds: in the case of an atmosphere with solar or $10\times$ solar abundance, an opaque cloud deck as high as $2.9 R_{\oplus}$ ($\sim 100 \text{ mbar}$; cf. Figure 1) still allows us to detect the spectroscopic signature of the planet.

The closest we come to detecting any atmospheric model (i.e., those tests which result in the

largest values of ΔBIC and $\sum\text{DCF}_0$) are our no-methane and low-carbon models. The no-methane model (cf. Figure 13) is the only model with a broadband ($|v_{lag}| \leq 200 \text{ km s}^{-1}$) sum greater than zero, but it is still consistent with zero at the 0.7σ level. Cross-correlation with the low-carbon model (cf. Figure 14) produces a very interesting feature, similar in size and shape to the expected narrowband signal but offset by 20 km s^{-1} . This large cross-correlation lag seems too large to be explained by either uncertainties in GJ 1214b’s orbit or in our wavelength calibration. Since this feature is only discrepant from zero at the 1.9σ level, both these low-significance $\sum\text{DCF}$ measurements seem most likely to be simple false positives. Nonetheless, these low-methane models remain intriguing in light of the correspondence between their predicted planetary radii and recent photometric observations (as we describe below).

5.2. Constraints on GJ 1214b’s atmosphere

If GJ 1214b has a H_2/He -dominated atmosphere, our observations require a reduced methane abundance in order for the atmospheric signature to remain undetectable to our analysis. Such an atmosphere also resolves the tension between the recent claims of a high (Bean et al. 2010; Désert et al. 2011) and low (Croll et al. 2011b) mean molecular weight atmosphere on GJ 1214b. Zahnle et al. (2009) has suggested that the atmospheres of cooler (but still strongly irradiated) planets may be conducive to photochemistry and polymerization of CH_4 into more complex organic compounds, which may form a haze with significant optical opacity. An optical haze (as observed on HD 189733b; Sing et al. 2011) formed from CH_4 reaction products provides a possible way to reconcile the nearly flat optical (Bean et al. 2010) transmission spectrum with the significantly larger Ks-band radius (Croll et al. 2011b).

Thus a methane-depleted, H_2/He -dominated atmosphere with an optical haze appears broadly consistent with all of the optical and infrared results for this system. Intriguingly, the only two atmospheric models to evince even a hint of a detected signal in our spectroscopic analysis have little or no methane; these are the models with low carbon and zero methane abundances (cf. Table 4, and Figures 13 and 14); the correspondence is curious and warrants further consideration. As Figure 15 demonstrates, both of these models are consistent (within $\sim 1.5\sigma$) with the observed mid- and near-infrared planetary radius ratios (Désert et al. 2011; Croll et al. 2011b) – compare this to the equilibrium-abundance models ruled out by our analysis, which are also discrepant (at $> 5\sigma$) from the photometric observations. Further observations are certainly needed. Fortunately, a methane-depleted atmosphere should be easy to characterize since it should still exhibit prominent absorption features from H_2O . To disentangle the effects of these exoplanetary absorption features from the telluric H_2O that defines the edges of ground-based observing bands, the atmosphere might best be characterized from space using the HST WFC3 grism in the J and H bands; ground-based narrowband infrared transit photometry (e.g., $2.1\text{-}2.3 \mu\text{m}$) could also test the existence of such an atmosphere.

A number of possible interpretations consistent with our results and with other observations are excluded solely by the large Ks transit depth (Croll et al. 2011b). For example, our data alone are consistent with a dense molecular (non- H_2) atmosphere on GJ 1214b, which would reduce the atmospheric scale height such that the transmission spectrum would be essentially constant with wavelength. This is consistent with the near-constant optical and mid-infrared transit depth (Bean et al. 2010; Carter et al.

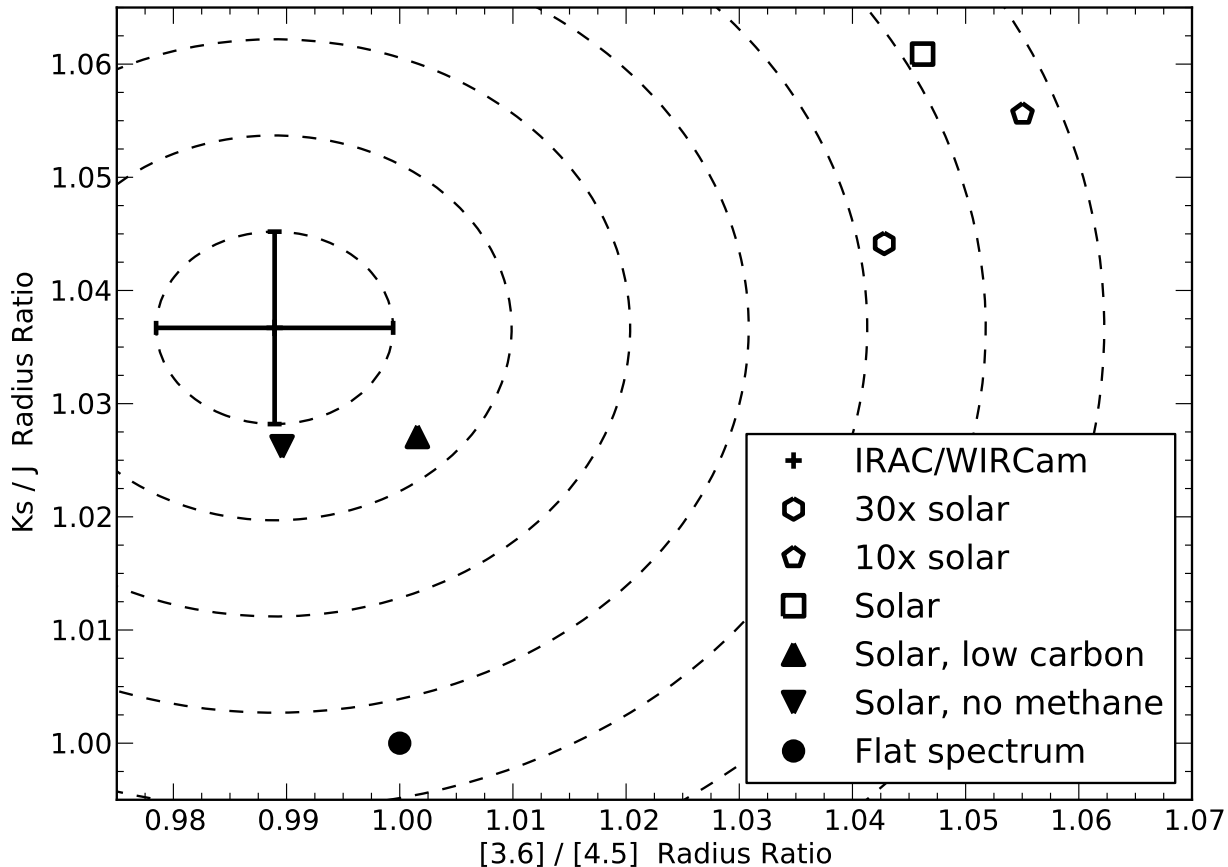


Fig. 15.— Near-infrared (K_s/J) and mid-infrared ($[3.6]/[4.5]$) planetary radius ratios for GJ 1214b. Values predicted by our atmospheric models, and the observed ratios and their uncertainties as measured with IRAC (Désert et al. 2011) and WIRCam (Croll et al. 2011b), are plotted. Dashed lines are the photometric error ellipses at intervals of 1σ . Solid symbols are models consistent with our analysis; open symbols are models that we rule out. Models substantially depleted in methane are consistent with our and prior observations, but equilibrium-abundance H_2/He -dominated models are strongly inconsistent with all observations. A flat transmission spectrum (due, e.g., to an atmosphere dominated by heavier molecular species), though consistent with our spectroscopic analysis, is inconsistent with photometric observations at $> 4\sigma$.

2010; Désert et al. 2011). This scenario would imply that GJ 1214b probably did not accrete much of its atmosphere from the gaseous protoplanetary disk in which it presumably formed, but instead formed largely from accretion of, and outgassing by, volatile-rich ices (Rogers & Seager 2010). Such an atmosphere would have features in transmission an order of magnitude weaker than those expected for a H_2/He -dominated atmosphere, and so would be more amenable to characterization by looking for the $\lesssim 10^{-3}$ mid-infrared ($>5 \mu m$) secondary eclipse signature (Miller-Ricci & Fortney 2010). Such observations may have to wait for the James Webb Space Telescope, though perhaps dedicated observations with the Stratospheric Observatory for Infrared Astronomy (SOFIA) could make a contribution

somewhat sooner.

GJ 1214b’s atmosphere would also be consistent with our observations if it were covered in high-altitude ($> 2.9 R_{\oplus}$ or < 100 mbar) clouds that would mask the spectroscopic signals to which we are sensitive. However, the effect of such a cloud layer would presumably extend to the optical, where observations demonstrate that the planet is significantly smaller than this. This discrepancy suggests that in a H_2/He -dominated atmosphere clouds could not consistently explain our (and prior) results.

In our calculations we have assumed a near-infrared planetary radius of $\sim 2.8 R_{\oplus}$, corresponding to $R_P/R_* \sim 0.12$. It is possible that the radius of the host star GJ 1214 has been overestimated by as much as $\sim 15\%$ (Charbonneau et al. 2009; Carter et al. 2010), making any planetary atmosphere more difficult for us to detect. A smaller radius would increase the surface gravity and decrease the atmospheric scale height, and a higher density would make the planet somewhat more consistent with denser interior models that may be less likely to host the extended, H_2/He -dominated envelopes to which our observations are most sensitive. This reduced radius would allow GJ 1214b’s mass and radius to be fit without any atmosphere whatsoever (even the larger radius is only 2σ discrepant from such a scenario Rogers & Seager 2010). Though it may be difficult to motivate a formation and evolution scenario that leads to a composition wholly lacking an atmosphere, this would be consistent with most current observations – except, once again, for the Ks band transit measurements (Croll et al. 2011b) which seems to argue against all scenarios but those with H_2/He -dominated atmospheres.

5.3. Lessons for future ground-based spectroscopy

High-resolution spectroscopy holds promise for the characterization of extrasolar atmospheres, as evidenced by the limits we set here with only half a night’s observations. Throughout this paper, we have noted that our analysis is sensitive to variations in transit depth with wavelength, and not to the absolute transit depth. A simple way to quantify our final sensitivity is in terms of the level of radius variability we can rule out, as measured by σ_{R_P} , the standard deviation of $R_P(\lambda)$ at our model resolution. Though the details of our sensitivity analysis depend on the shape of the spectrum being tested, a simple rule of thumb turns out to work fairly well: as seen from Table 4, we can reliably detect models with $\sigma_{R_P} \gtrsim 0.05 R_{\oplus}$. Equivalantly, any tested model with wavelength-dependent transit depth variations $\gtrsim 5 \times 10^{-4}$ over our wavelength range should be detectable to our analysis. Successful characterization with NIRSPEC of a 100% H_2O atmosphere on a GJ 1214b-like planet would require a factor of ~ 5 better precision, which seems at the outer edge of what might be achieved with a dedicated spectroscopic campaign. The atmospheres of smaller, cooler, and more Earth-like planets will be even more challenging to detect. On the other hand, a GJ 436b-like Hot Neptune would have an atmospheric signal only a factor of two below our sensitivity, and so such an object might be amenable to high-resolution spectroscopic characterization in only a single observing season.

Our sensitivity is fundamentally limited by the spectrophotometric variability resulting from (a) variations in spectroscopic slit loss, (b) telluric-induced flux variations, and (c) slow drifts likely of instrumental or residual telluric origin. We address the first by removing the common-mode slitloss term (removing the absolute transit depth from our data), the second by calibrating our data with various empirical airmass terms, and the third by including low-order polynomials in our fitting process; our

ability to address these suggests that further observations with NIRSPEC or comparably instruments would probably allow us to probe a somewhat greater region of atmospheric parameter space and should not be discounted. We are aware of at least one other group which has obtained NIRSPEC K band observations of GJ 1214b during transit, and we look forward to seeing whether these can help to more tightly constrain the model parameter space we have explored.

That said, we note that concerns (a) and (b) above can be largely eliminated – without the penalties or tradeoffs incurred by our methods – by multi-object spectroscopy (Bean et al. 2010); this technique would at least partially mitigate limitation (c) as well. There are a growing number of cryogenic, infrared multi-object spectrographs on large-aperture telescopes: MOIRCS at Subaru, and soon MOSFIRE at Keck and FLAMINGOS-2 at Gemini South. Combined with extant optical multi-object spectrographs these instruments may have a leading role to play in the future characterization of exoplanetary atmospheres.

A subset of exoplanet systems could be amenable to spectroscopic characterization in an alternate manner. If an exoplanet host star has another star of comparable brightness nearby, observations from a sufficiently precise slit-viewing camera or facility guiding camera could be used to calibrate out the (broadband) photometric variations resulting from telluric effects. With a sufficiently wide spectrograph slit (probably $\geq 3''$), good guiding, and no slit nodding the slit loss term that limits our observations here could also be almost wholly compensated for. This method could enable at least coarse spectroscopic characterization on even smaller (and hence, more accessible) telescopes, and we plan to test it in future observations.

6. Conclusions

Planets with GJ 1214b’s mass and radius have no solar system analogues, so *a priori* we know relatively little about the nature of their interiors or atmospheres. Here we report high-resolution near-infrared spectroscopy of the GJ 1214 system during GJ 1214b’s transit, taken to ascertain the nature of the planet’s atmosphere. Calibration using a common-mode flux variation time series (which removes the absolute transit depth, C , from the data) allows us to search for the relative change in transit depth with wavelength: that is, we measure the quantity $(R_P(\lambda)/R_*)^2 - C$.

Our spectroscopy rules out a clear, cloudless atmosphere in or near chemical equilibrium for GJ 1214b assuming solar, $10\times$ solar, and $30\times$ solar abundances, and in this sense we are consistent with previous results (Bean et al. 2010; Désert et al. 2011). Our data are consistent with any of the following: (i) a H_2/He -dominated atmosphere depleted in methane, (ii) an atmosphere dominated by heavier molecular species with a smaller atmospheric scale height, or (iii) almost any atmospheric composition if obscured by a high-altitude cloud layer. However, the large Ks band transit depth reported for this system (Croll et al. 2011b) argues against (ii) and (iii) above. GJ 1214b thus appears more likely to be a scaled-down version of GJ 436 b (another methane-depleted, H-dominated planet orbiting an M dwarf) than a rock- or ice-dominated body with a dense envelope. As the interpretation hinges largely on the Ks measurement, further observations of this system are needed to pin down the nature of its atmosphere.

Planet surveys suggest that objects of this mass and size may be quite common (Howard et al. 2010;

Borucki et al. 2011), so we expect similar planets to be confirmed in the future. Further observations of GJ 1214b during transit – both photometric and spectroscopic – will help refine our understanding of this object and future objects like it, and pave the way toward the characterization of ever more Earthlike planets. Because GJ 1214 is such a cool star, infrared wavelengths continue to offer the best prospects for these future observations. We suggest that infrared spectroscopy (especially from spectrographs such as Subaru/MOIRCS, Keck/MOSFIRE, and HST/WFC3) and narrowband photometry will be able place the tightest atmospheric constraints on this planet and those like it as yet undiscovered.

7. Acknowledgements

Support for this work at UCLA was provided by NASA through awards issued by JPL/Caltech and the Space Telescope Science Center. TB is supported by a NASA Origin of Solar Systems grant awarded to Lowell Observatory. We thank I. McLean for useful discussions about the NIRSPEC instrument, and D. Rodriguez for helpful comments during manuscript preparation.

The data presented herein were obtained at the W.M. Keck Observatory, which is operated as a scientific partnership among the California Institute of Technology, the University of California and the National Aeronautics and Space Administration. The Observatory was made possible by the generous financial support of the W.M. Keck Foundation. The authors wish to recognize and acknowledge the very significant cultural role and reverence that the summit of Mauna Kea has always had within the indigenous Hawaiian community. We are most fortunate to have the opportunity to conduct observations from this mountain.

REFERENCES

- Andrae, R. 2010, ArXiv e-prints, [ADS, 1009.2755](#)
- Asplund, M. 2005, ARA&A, 43, 481, [ADS](#)
- Barman, T. 2007, ApJ, 661, L191, [ADS, 0704.1114](#)
- Barman, T. S., Hauschildt, P. H., & Allard, F. 2005, ApJ, 632, 1132, [ADS, arXiv:astro-ph/0507136](#)
- Barnes, J. R. et al. 2010, MNRAS, 401, 445, [ADS, 0909.2510](#)
- Barnes, J. R., Leigh, C. J., Jones, H. R. A., Barman, T. S., Pinfield, D. J., Collier Cameron, A., & Jenkins, J. S. 2007, MNRAS, 379, 1097, [ADS, 0705.0272](#)
- Bean, J. L., Miller-Ricci Kempton, E., & Homeier, D. 2010, Nature, 468, 669, [ADS, 1012.0331](#)
- Borucki, W. J. et al. 2011, ArXiv e-prints, [ADS, 1102.0541](#)
- Carter, J. A., Winn, J. N., Holman, M. J., Fabrycky, D., Berta, Z. K., Burke, C. J., & Nutzman, P. 2010, ArXiv e-prints, [ADS, 1012.0376](#)
- Charbonneau, D. et al. 2009, Nature, 462, 891, [ADS, 0912.3229](#)
- Claret, A. 2000, A&A, 363, 1081, [ADS](#)
- Croll, B., Lafreniere, D., Albert, L., Jayawardhana, R., Fortney, J. J., & Murray, N. 2011b, AJ, 141, 30, [ADS, 1009.0071](#)
- Croll, B., Albert, L., Jayawardhana, R., Miller-Ricci Kempton, E., Fortney, J. J., Murray, N., & Neilson, H. 2011a, ArXiv e-prints, [ADS, 1104.0011](#)
- Deming, D., Brown, T. M., Charbonneau, D., Harrington, J., & Richardson, L. J. 2005, ApJ, 622, 1149, [ADS, arXiv:astro-ph/0412436](#)

- Désert, J. et al. 2011, ArXiv e-prints, [ADS](#), [1103.2370](#)
- Donati, J., Semel, M., Carter, B. D., Rees, D. E., & Collier Cameron, A. 1997, MNRAS, 291, 658, [ADS](#)
- Edelson, R. A., & Krolik, J. H. 1988, ApJ, 333, 646, [ADS](#)
- Gillon, M. et al. 2007, A&A, 471, L51, [ADS](#), [0707.2261](#)
- Hinkle, K. H., Wallace, L., & Livingston, W. 2003, 35, 1260, [ADS](#)
- Howard, A. W. et al. 2010, Science, 330, 653, [ADS](#), [1011.0143](#)
- Irwin, J., Charbonneau, D., Nutzman, P., & Falco, E. 2009, in IAU Symposium, Vol. 253, IAU Symposium, 37–43, [0807.1316](#), [ADS](#)
- Jolliffe, I. T. 1986, Principal Component Analysis, ed. Jolliffe, I. T.
- Lord, S. D. 1992, A new software tool for computing Earth’s atmospheric transmission of near- and far-infrared radiation, Tech. rep., [ADS](#)
- Madhusudhan, N., & Seager, S. 2009, ApJ, 707, 24, [ADS](#), [0910.1347](#)
- Mandel, K., & Agol, E. 2002, ApJ, 580, L171, [ADS](#)
- Mandell, A. M., Drake Deming, L., Blake, G. A., Knutson, H. A., Mumma, M. J., Villanueva, G. L., & Salyk, C. 2011, ApJ, 728, 18, [ADS](#), [1011.5507](#)
- McLean, I. S. et al. 1998, in SPIE Conference Series, ed. A. M. Fowler, Vol. 3354, 566–578, [ADS](#)
- Miller-Ricci, E., & Fortney, J. J. 2010, ApJ, 716, L74, [ADS](#), [1001.0976](#)
- Miller-Ricci, E., Seager, S., & Sasselov, D. 2009, ApJ, 690, 1056, [ADS](#), [0808.1902](#)
- Nettelmann, N., Fortney, J. J., Kramm, U., & Redmer, R. 2010, ArXiv e-prints, [ADS](#), [1010.0277](#)
- Redfield, S., Endl, M., Cochran, W. D., & Koesterke, L. 2008, ApJ, 673, L87, [ADS](#), [0712.0761](#)
- Rogers, J. C., Apai, D., López-Morales, M., Sing, D. K., & Burrows, A. 2009, ApJ, 707, 1707, [ADS](#), [0910.1257](#)
- Rogers, L. A., & Seager, S. 2010, ApJ, 716, 1208, [ADS](#), [0912.3243](#)
- Rojas-Ayala, B., Covey, K. R., Muirhead, P. S., & Lloyd, J. P. 2010, ApJ, 720, L113, [ADS](#)
- Schlaufman, K. C., & Laughlin, G. 2010, A&A, 519, A105+, [ADS](#), [1006.2850](#)
- Sing, D. K. et al. 2011, ArXiv e-prints, [ADS](#), [1103.0026](#)
- Snellen, I. A. G., de Kok, R. J., de Mooij, E. J. W., & Albrecht, S. 2010, Nature, 465, 1049, [ADS](#), [1006.4364](#)
- Swain, M. R. et al. 2010, Nature, 463, 637, [ADS](#), [1002.2453](#)
- Vacca, W. D., Cushing, M. C., & Rayner, J. T. 2003, PASP, 115, 389, [arXiv:astro-ph/0211255](#)
- Zahnle, K., Marley, M. S., & Fortney, J. J. 2009, ArXiv e-prints, [ADS](#), [0911.0728](#)